High-yield cellulose hydrolysis by HCl vapor: cocrystallization, deuterium accessibility and hightemperature thermal stability

Jonathan Leboucher, Philippe Bazin, Didier Goux, Hussein El Siblani, Arnaud Travert, Antoine Barbulée, Joel Bréard, Benoît Duchemin

High-yield cellulose hydrolysis by HCl vapor: co-crystallization, deuterium accessibility and high-temperature thermal stability

Jonathan Leboucher[a,d], Philippe Bazin[b], Didier Goux[c], Hussein El Siblani[b,] Arnaud Travert[b], Antoine Barbulée[d], Joel Bréard[a], Benoit Duchemin[a,*]

[a] Normandie Univ, ULH, CNRS, LOMC, 76600 Le Havre, France
[b] Normandie Univ, ENSICAEN, UNICAEN, CNRS, LCS, 14000 Caen, France
[c] Normandie Univ, UNICAEN, CMABio3 FF 4206 ICORE, 14000 Caen, France
[d] Groupe Depestele, BP 21, 14540 Bourguébus, France

* benoit.duchemin@univ-lehavre.fr (corresponding author)

Abstract

Hydrochloric acid hydrolysis in its gas form was used to produce cellulose nanoparticles from flax shives with a very high yield (> 90%). The efficiency of the transformation was examined by gravimetry, atomic force microscopy and transmission electron microscopy. A novel purpose-built anisotropic line-broadening X-ray diffraction model was used. This XRD method uses a parametric shape in order to address the issue of strongly broadened and overlapping Bragg rays that are characteristic of nano-sized crystallites. This method demonstrated the remarkable stability of the crystallite shapes during hydrolysis and its sensibility was sufficient to detect a minor co-crystallization along the hydrophilic faces. The presence of amorphous material *stricto sensu* in the form of individual and randomly oriented chains was not necessary to describe the diffractograms accurately. Thermal FTIR with isotopic exchange was also performed using deuterium oxide to characterize the accessibility of the materials between 20 and 260°C. Further, back-exchange experiments were performed in order to quantify the hysteretic amount of deuterium that was trapped by microstructural reorganization. These experiments showed that hydrolysis cancelled any form of deuterium trapping (water-induced co-crystallization). For the first time, thermal FTIR demonstrated that isotopic labelling of cellulose sources can produce false positives when conducted at room temperature and thermal FTIR can unambiguously distinguish between labelled cellulose groups and free deuterium oxide, which is paramount when measuring the higher accessibility of the nanocelluloses. It was also demonstrated that the high-temperature hydrogen bond reorganization and thermal degradation of the cellulose chains strongly depend on the hydrolysis and on the microstructure of the substrate.

Introduction

Cellulose nanocrystals (CNC) are needle-like organic crystals that can be extracted from the lignocellulosic biomass. CNC may be useful in multiple applications. For instance, they can reinforce polymer matrices and improve their stiffness, damping, oxygen barrier properties or provide shape-memory effects.(Eichhorn et al. 2010; Klemm et al. 2011; Dufresne 2013; Lourdin et al. 2016) Multiple applications in the field of functional materials exist: CNC can for instance be used as photonic materials, biocatalysts, conductive materials, biosensors or crack-healing drilling fluids.(Lam et al. 2012; Lin et al. 2012)

The mass-production of CNC is limited by the yield of current production methods. The most common preparation method of CNC is a sulfuric acid hydrolysis. Initially, this process was proposed by Rånby 70 years ago (Rånby et al. 1949) and has since been improved to enhance the final yield of CNC. For instance, yields as high as 66-69% for wood-based CNC were expected, based on the results of a central composite design study.(Dong et al. 2016) A predicted maximum yield of 54% was announced for CNC made from microcrystalline cellulose using surface response methodology.(Bondeson et al. 2006) It has also been demonstrated that other acids could successfully hydrolyze cellulose. For instance, hydrochloric acid, formic acid, phosphoric acid, bromhydric acid or phosphotungstic acid can be used.(Nevell and Upton 1976; Habibi et al. 2010; Yu et al. 2013; Camarero Espinosa et al. 2013; Liu et al. 2014; Li et al. 2015; Du et al. 2016) In particular, the yield of CNC produced using $FeCl_3$-catalyzed formic acid can reach values of 75% and the yield of CNC using an hydrothermal hydrolysis pathway in HCl can reach 93%. However, a recent breakthrough regarding the yield of the acid hydrolysis was recently reported.(Kontturi et al. 2016; Lorenz et al. 2017; Pääkkönen et al. 2018) Instead of using conventional "wet-chemistry" reaction pathways, this method exposes cotton cellulose to a vapor of HCl. An impressive yield of 97-99% could be achieved and the neutralization of the acid was tremendously simplified. In comparison with the classical sulfuric acid method, HCl hydrolysis produces CNC that have a lower amount of surface charges, which leads to an unstable colloidal dispersion but to a better thermal stability of the dry particles (Araki et al. 1998; Klemm et al. 2011; Dufresne 2013; Fang et al. 2016; Kontturi et al. 2016; Lorenz et al. 2017). The HCl vapor process also uses less water and practically solves the issues surrounding the recycling of the acid at the end of the process.(Kontturi et al. 2016; Lorenz et al. 2017; Niinivaara et al. 2018)

The hydrolysis of cellulose with HCl needs to be well-understood in order to control some important parameters such as the dimensions of the CNC or their redispersibility in various solvents.(Kontturi et al. 2016; Lorenz et al. 2017) So far, it has been demonstrated that HCl hydrolysis in the vapor phase induces the adsorption of a monolayer of HCl molecules on the surface of the solid cellulosic substrate, at a concentration above the water solubility limit.(Kontturi et al. 2016; Niinivaara et al. 2018; Pääkkönen et al. 2018) However, the presence of residual water is paramount to dissociate the HCl molecules and proceed with the hydrolysis.(Pääkkönen et al. 2018) Hydrolysis consists in a scission of the cellulose chains and it yields a marginal quantity of glucose. Since there is no mass transfer during the exposure to the acidic vapor, the glucose is rinsed away when the hydrolysis is quenched by immersing the substrate in water.(Niinivaara et al. 2018) It is also well established that the degree of polymerization (DP) decreases non-linearly with the duration of the hydrolysis. The depolymerization kinetics is well-described by a two-stage model (first order kinetic).(Calvini et al. 2007; Pääkkönen et al. 2018) In the early stages of the hydrolysis, the DP undergoes a fast decrease that is mostly assigned to the hydrolysis of the 1,4 glycosidic bonds of the readily accessible regions.(Battista et al. 1956; Kontturi et al. 2016; Niinivaara et al. 2018) After long hydrolytic processes, the amount of chain scission reach a plateau value that is characterized by a "level-off DP" (LODP).(Battista et al. 1956; Calvini 2005; Kontturi et al. 2016) An increased exposure to HCl leads to a slow DP reduction consistent with an endwise

2

depolymerization of the low DP paracrystallites or segments.(Pääkkönen et al. 2018) Kinetic studies can be completed by microscopy studies. It was demonstrated by AFM that HCl hydrolysis performed on carboxylated cellulose nanofibrils occurs preferentially at kinks.(Nyström et al. 2018) Kinks in cellulose nanofibers are best described as crystalline defects, rather than amorphous regions.(Nishiyama et al. 2003; Usov et al. 2015) Therefore, previous results agree on the deterministic nature of HCl hydrolysis: this type of hydrolysis will preferentially target the water-accessible regions and the kinks that are located along the nanofibril length. On the other hand, it is still unclear whether a possible recrystallization of cellulose when exposed to an HCl vapor could play a role. This work hypothesis was put forward to explain the high yields of the HCl vapor method, the slight crystallinity increase and the moderate crystallite thickening observed by solid-state NMR and X-ray diffraction.(Kontturi et al. 2016) It is indeed possible to envisage some level of recrystallization once the fibrillar structure of the cellulosic substrate is hydrolyzed: chains that were previously structurally constrained become free to reorder once split into smaller fragments. Nevertheless, the moderate crystallinity increase of the product after it was fragmented to CNC and the exceptionally high yield of the method challenge our conception of CNC: should CNC be considered as single nanocrystals, or as rigid, hydrolytically stable fragments bearing some structural disorder?

In the present work, cellulose nanocrystals were produced with a high yield from chlorine-free bleached flax shives, using the HCl vapor method proposed by Kontturi *et al.*(Kontturi et al. 2016) In the past, CNC have been produced from unbleached flax shives - vascular bundles (phloem and xylem) akin to normal wood tissues - using the ammonium persulfate method.(Leung et al. 2011) . The hydrolysis time was varied and the resulting nanoparticles were characterized in terms of width, length and thickness using TEM and AFM. WAXD was used to determine the size and shape of the nanocrystals under the assumption of a bimodal size distribution and taking into account possible I_α/I_β stacking faults. Eventually, an isotopic exchange monitored by an ATR-FTIR analysis from room temperature to 260°C was performed in order to quantify the water accessibility and the structural changes undergone by the cellulose during this HCl hydrolysis. To the best of our knowledge, the combination of isotopic labelling and high-temperature FTIR analysis has never been performed on such materials. The production of uncharged cellulose nanoparticles with a high yield gives us an opportunity to gain further understanding as to the novel production method using gaseous HCl as well as a better insight into the nanocellulose structure itself.

Experimental section

Materials

Flax shives were provided by SAS Teillage Vandecandelaere (Depestele company), located in Bourguébus (Normandy, France). Flax shives were ground and sieved with a 315 μm mesh. The flax shives were bleached and the procedure as well as the analytical results (POM, SEM, WAXD, ATR-FTIR and ^{13}C CP/MAS ss-NMR) are given in supplementary information. Deuterium oxide (D$_2$O, 99.8% atom D, Roth), toluene (≥ 99.5%, AnalaR normapur, VWR), absolute ethanol (≥ 99.5%, empura, Merck), sodium hydroxide (NaOH, ≥ 99%, Carl Roth), hydrogen peroxide (35 %, stabilized aqueous solution, Alfa Aesar), hydrochloric acid (32% for analysis, emsure, Merck) and deionized water (18.2 *MΩ*cm*) were used as received. Filtrations were made on filter paper (Whatman n°1) unless otherwise stated. Glass fiber filters (90 mm diameter, MN85/70, Macherey-Nagel) and nylon filters (0.45 μm pore size, 90 mm diameter, Whatman) were also used for filtration purposes.

Methods

Acid hydrolysis

Bleached flax shives were suspended in deionized water (2.1 wt. %) and mixed with an Ultraturrax (IKA) for 3 minutes at 7,000 rpm and 2 minutes at 11,000 rpm. The suspensions were filtered on a nylon filter in order to produce a film with an even thickness for subsequent hydrolysis. After filtration, the films were dried at ambient conditions under a fume hood. The films were then separated from the nylon filter. The bottom of a vacuum desiccator was filled with hydrochloric acid (80 ml in a desiccator 100 mm in diameter). In order to reach an equilibrium (P_{HCl} = 2.9 kPa), the valve of the desiccator was left open for 2 days. It was then shut one day before the start of the hydrolysis experiment. The cellulose films (~1.0 g; water content: 30 ± 6 wt. %) were introduced in the desiccator (Table S2). Hydrolysis was performed for 30 min, 1 h, 2 h, 4 h and 8 h. A chemical quench was performed in deionized water (250 mL) in order to stop the hydrolysis. The hydrolyzed material was then filtered and suspended again in 250 mL of deionized water. The suspension was dispersed with high intensity ultrasounds (Bioblock Scientific, model vibracell 75115, 500 W, 20 kHz) set at 40% output power with 100 min of treatment time (3 s on, 2 s off). The average energy transmitted to the solution was 171 ± 5 kJ. A sample of reference (control sample) was also produced using the same protocol with the exception of the hydrolysis.

Characterization

X-ray diffraction

Measurements

Powder diffractograms were acquired in reflection mode with a θ-θ Bragg-Brentano configuration using an Xpert-Pro Powder (PANalytical B.V., Almelo, Nederland) with a cobalt radiation source ($\lambda_{CoK\alpha}$ = 1.790307 Å) and a PIXcel 1D detector. The operating voltage and current were maintained at 40 kV and 40 mA, respectively. Measurements were made between 10 and 80° with 0.0131° steps and for a total duration of 8 h. The lateral divergence of the incident beam path was controlled with 0.04° Soller slits and a 10 mm mask. The divergence in the 2.θ plane was controlled with a ½° fixed slit.

Anisotropic size broadening

The results were analyzed using a Rietveld method that was adapted from a recently published work.(Duchemin 2017b) This method describes the cellulose I_β crystallites as anisotropic crystallites with a deterministic shape and size in the direct space. The method was slightly modified in the present work to provide a more accurate three-dimensional description of the crystallites. The anisotropic size distribution is described in the direct space by a parametric superellipsoid hull obeying the following equation set:

$$x = r_x.sign(cos\omega.sin\chi).|sin\chi|^m.|cos\omega|^n \qquad (1)$$
$$y = r_y.sign(sin\omega.sin\chi).|sin\chi|^m.|sin\omega|^n \qquad (2)$$
$$z = r_z.sign(cos\chi).|cos\chi|^m \qquad (3)$$

With $\omega \in [-\pi ; \pi [$ and $\chi \in [-\pi ; \pi [$. The x axis (resp. z) is oriented along the crystallographic *a* (resp. *c*) axis. Additionally, *m* (resp. *n*) is the "squareness" parameter in the z (resp. x and y) axis. Values close to 0 describe a square shape, a value of 1 describes a perfect ellipsoid, a value of 2 describes a "diamond shape" (rhombus) and values > 2 create a recess between the corners of this rhombus; all intermediary values are adequate.(Duchemin 2017b) For each diffracting crystallographic plane (*hkl*), the diameter of the crystallites in the direction orthogonal to the plane is:

$$d_{hkl} = 2\sqrt{x^2 + y^2 + z^2} \qquad (4)$$

The link between the FWHM of the Bragg band and d_{hkl} is given by Scherrer equation with a value K = 0.9.(Guinier 1963; Duchemin 2017a) Therefore, a homothetic relationship is found between the 3D shape of the particles and the FWHM spectrum of the diffractogram. For each (*hkl*) pane, there exists a vector $\boldsymbol{n}^{hkl}$ normal to this plane that obeys the equation:

$$\boldsymbol{n}^{hkl} = \begin{pmatrix} n_x^{hkl} \\ n_y^{hkl} \\ n_z^{hkl} \end{pmatrix} = \alpha . \begin{pmatrix} x \\ y \\ z \end{pmatrix} \qquad (5)$$

The vector $\boldsymbol{n}^{hkl}$ is a function of the lattice parameters of the Iβ phase and it is expressed in the direct space $\mathbb{R}^3$. The equation set is solved algebraically to determine α, ω and χ for each plane, as a function of the five superellipsoid parameters. Therefore, solving the size and shape problem of an experimental diffractogram requires determining the values of r_x, r_y, r_z, m and n. This can easily be performed using the least-square method to minimize the difference between the experimental diffractograms and their models. The parametric shape representation was plotted using the matplotlib and numpy Python libraries.

Implementation and triphasic model

The signal was defined as the sum of three components: a background, small diffusing domains of cellulose IV$_I$ with no more than 2-3 chains in thickness, and larger cellulose Iβ crystallites, usually in the 25-60 Å diameter range.(Duchemin 2017b) The background comprised a Gaussian halo centered at 2.θ = 0° and a zero-order background; this form essentially captures the main background contributions: incoherent (Compton) scattering, coherent scattering and air scattering.(Ramírez and Bucio 2018) Cellulose IV$_I$ is selected as a disordered form of cellulose Iβ, as discussed in previous works.(Marrinan and Mann 1956; Wada et al. 2004; Newman 2008; Duchemin 2017b) The preferred orientation of cellulose Iβ was modelled in a simple manner using the March-Dollase approach along the $\boldsymbol{c}$ axis.(Duchemin 2017b)

Furthermore, the amount of I$_\alpha$/I$_\beta$ stacking faults was estimated using the structure factor list published by Driemeier and Francisco in their seminal work using the Diffax software.(Driemeier and Francisco 2014) These structure factors were integrated in our analysis. The problem was solved on a desktop workstation using the Microsoft® Excel Solver Add-in and the least-square method. The following parameters were refined for cellulose Iβ: lattice dimensions, monoclinic angle, March-Dollase strength, relative phase intensity, r_x, r_y, r_z, m, n and the amount of stacking faults. The parameters relative to cellulose IV$_I$ crystallites that were refined were their relative amount and width of crystallites. As to the background, the height and width of the central Gaussian function and the zero-order function were refined. The refinements were run until a variation of the correlation coefficient < 1 ‰ between the experimental data and the simulated ones was obtained.

ζ potential

The ζ potential was measured with a Zeta Sizer Nano-Z, with a Dip Cell (Malvern Instrument, Malvern UK). Measurements were repeated 5 times and the solid particle concentration amounted to 0.1 g.L^{-1}. The results were analyzed with the proprietary software (version 7.11, Malvern, UK) and Schmoluchowski equation.

Atomic force microscopy

The cellulose nanocrystals were imaged using an atomic force microscope (Innova, Brücker). Suspensions were diluted to 0.06 g.L^{-1}, a drop was cast on a freshly cleaved mica and the drop was allowed to dry. The scans were performed using the tapping mode in air. Ultrasharp tips (Tespa V2, Brüker, 320 kHz, 42 N/m, 7 nm tip radius) were used. The height of the CNC was measured using the software Nanoscope analysis (Brücker).

Transmission electron microscopy

The width and length of the CNC were measured by transmission electron microscopy using a Jeol JEM-1011 TEM equipped with a tungsten filament at 80.0 kV acceleration voltage. Copper grids covered by a formvar film (0.5% in dichloromethane) were used. The grids were also placed in a glow discharge (Elmo, Cordouan Technologies) before suspension casting.

Each suspension (0.06 g.L^{-1}) was dispersed with high intensity ultrasounds (Vibracell 75115) for 5 minutes (3s pulse on, 2s pulse off, 40% intensity, average energy: 13 367 J). One drop of 3 μl was then deposited on the grid. After 10 min, excess suspension was eliminated, 3 μl of uranyl acetate (1.5%) were put on the grid for 1 min in a black box. Excess was eliminated and the grids were dried under the fume hood. Two grids were made for each sample.

High temperature ATR-FTIR

All the samples were studied with an FTIR spectrometer (Nicolet iS50 FT-IR, Thermo scientific) equipped with a temperature-controlled ATR cell (diamond ATR "golden gate high temperature", SPECAC). The measurements were performed by applying a 2°C/min temperature ramp from room temperature to 260°C and one spectrum was recorded every 40s. Each spectrum resulted from the accumulation of 64 scans at a 4 cm^{-1} resolution. The acquisition was done using the OMNIC (v.9.6) software. One spectrum was always acquired after a return to room temperature. The background was also measured at all temperatures on an empty cell in order to correct the temperature-induced background shifts. The plots of the raw data plots were performed using the Python libraries matplotlib and numpy. The data treatment was performed using the spectroscopy plugin implemented in Orange.(Demšar et al. 2013)

The measurements were performed on the non-hydrolyzed sample and on the hydrolyzed samples. They were performed on (i) control samples (ii) deuterated samples and (iii) deuterated samples that were further back-exchanged with ultrapure ordinary water.

In order to perform the hydrogen-deuterium exchange, 0.1 g of never dried material (control sample and 8 h hydrolysis) was immersed in 5 mL of D$_2$O in a 25 ml sealed glass bottle and the bottle was placed in an ultrasonic bath (VWR, 160 W) for 1 h. The suspension was then centrifuged and the supernatant was discarded. A fresh amount (5 mL) of D$_2$O was then added to the solid and the mixture was left in the ultrasonic bath for 4 h. This duration was found to be sufficient to reach a complete exchange of the accessible groups.(Mann and Marrinan 1956a, b, c) The solid substrate was again isolated by centrifugation. It was then dried overnight under a constant flux of dry N$_2$ (ultra-pure spectroscopy grade, purity > 99.999%) supplied by a Parker domnick hunter G1010E generator. Half of the dried deuterated mass was then swiftly placed in a chamber with a 75 % RH obtained by saturating D$_2$O with NaCl for one week. The chamber was sealed and reopened only for FTIR measurement purposes. The other half of the sample was reprotonated in order to assess the amount of deuterium trapped by drying hysteresis. To do so, the deuteration procedure was simply repeated by replacing D$_2$O with ultrapure H$_2$O. The sample was also stored in a sealed container with a known relative humidity (75% H$_2$O). Two "never deuterated" control samples were also produced by applying the same complete protocol with ultrapure H$_2$O.

A ratio of exchanged groups was calculated using the formula:

$$r_{access} = \frac{1.34 * A_{v_{OD}}}{1.34 * A_{v_{OD}} + A_{v_{OH}}} \qquad (6)$$

Where $A_{v_{OD}}$ is the area of the spectrogram taken between 2800 and 2360 cm^{-1} and $A_{v_{OH}}$ is the area of the spectrum taken between 3680 and 3050 cm^{-1}. The areas were measured after a linear baseline correction. 2-D correlation spectroscopy was not performed because of large band shifts. The formula is sometimes found without the 1.34 correction factor.(Horikawa et al. 2009; Thybring et al. 2017) This 1.34 factor stems from the v_{OH} to v_{OD} wavenumber shift after deuteration.(Hofstetter et al. 2006; Driemeier et al. 2015)   Indeed, since the band intensity is proportional to this wavenumber, a true measure of r_{access} requires this intensity correction to be performed.(Mann and Marrinan 1956b; Janoschek et al. 1978)

Results and discussions

Acid hydrolysis

    Yield, microscopy and ζ potential

The production of cellulose nanocrystals from bleached flax shives was performed with gaseous HCl for various durations, from 30 min to 8 h. The yields were characterized by a gravimetric method and were found to lie in the 89-92 wt.% range for all hydrolysis times (Table 1). A 2 wt.% weight loss was measured for the non-hydrolyzed sample which was attributed to the other processing steps (filtration, ultrasounds, *etc*). The nanocrystals were then observed using TEM and this technique was useful to assess their lengths and widths (Figure 1, left column). Generally speaking, the nanoparticles appeared as rods with "kinks" along their lengths. These kinks were observed in other works.(Nishiyama et al. 2003; Usov et al. 2015; Nyström et al. 2018) Nanoparticles with widths in the 10-22 nm range and with average lengths ranging from 160 to 800 nm were observed (Figure 2). These values decreased with the hydrolysis time but they were found to be relatively stable after 2 h of exposure to HCl (Figure 2). The dispersion of the data also decreased with time, probably due to the fractionation of the most refractory particles after longer exposure times to the acid vapor. The nanoparticles often appeared as aggregates of smaller nanocrystallites packed side-by-side. These nanocrystals were about 2-4 nm in width. Small disc-like fragments in the 10-35 nm diameter range were also sometimes observed (Figure 1). Due to their shape, these fragments can be attributed to remnants of lignin.(Beisl et al. 2017)

Atomic force microscopy can provide complementary information by giving an assessment of the height of the nanofragments as deposited on the mica substrates (Figure 1, right column). The values before hydrolysis are not reported because of the bias induced by the remnants of large (micron-sized) unaffected shives coexisting with scarce submicron microfibrils produced by the ultrasound treatment. The height of the nanoparticles evolved from ~30 nm after 30 min of hydrolysis to ~12 nm after 8 h. As observed using TEM, the average dimension was relatively stable after a 2 h hydrolysis (Figure 2), but the statistical dispersion was lower at 4 and 8 h. A 24 h hydrolysis was also trialed and no statistically significant evolutions of the dimensions were observed relative to the 8 h hydrolysis (results not shown). Both sets of results (TEM and AFM) underline the strong efficiency of the HCl vapor method when one wants to produce cellulose nanoparticles in a simple manner. Leung *et al.* (2011) reported the production of carboxylated cellulose nanocrystals from flax shives using ammonium persulfate (APS) in a one-pot method at 60°C for 16 h, without preliminary bleaching.(Leung et al. 2011) The nanocrystals produced in their work were thinner (5.1 ± 0.1 nm) and longer (296 ± 16 nm) at the expense of a lower yield: 22% when compared to 49% in this work (taking the bleaching step in consideration).
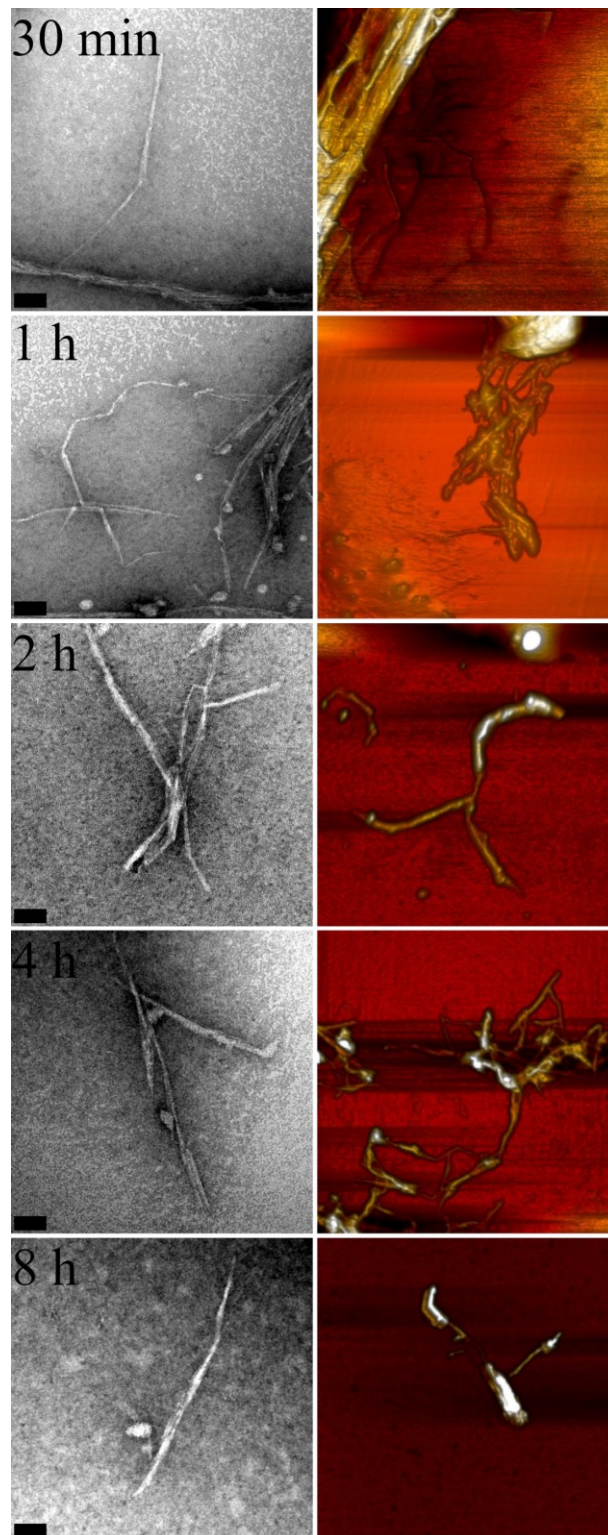
Figure 1. Transmission electron microscopy of CNC deposited on formvar films (left column, scale bars are 50 nm) and atomic force microscopy of CNC deposited on mica (right column, images are 2 μm x 2 μm).

.

Nanocrystals produced by sulfuric acid or APS bear repulsive surface charges due to the presence of grafted ionic groups. In general, the ζ-potential of such particles is much more negative than -20 mV and typically around -50 to -70 mV. In this work, the ζ-potential (> - 30 mV) resulting from the process is not sufficient to generate the required amount of electrostatic repulsion that would prevent the nanoparticles from aggregating (Table 1).

Therefore, the larger nanoparticle dimensions obtained in this work relative to those reported in the work of Leung *et al.* could be explained by the insufficient amount of electrostatic repulsion rather than by the amount of hydrolyzed material.(Leung et al. 2011) Lignin recondensation could also explain the increase of the ζ-potential after prolonged exposure to HCl vapors.(Pouteau et al. 2005; Papadopoulos et al. 2009)
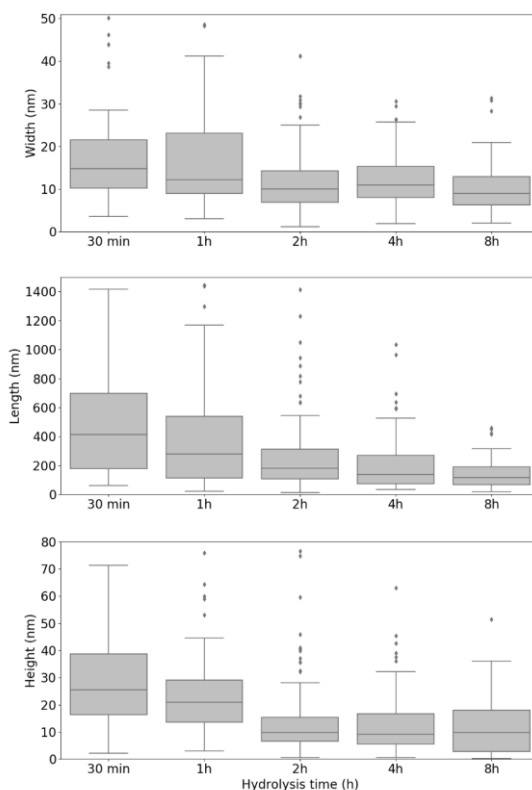

Figure 2. Box plots of the nanoparticle dimensions after various hydrolysis times. Length and width were measured by TEM whereas the height was measured by AFM.

Table 1. Summary of the dimensions (arithmetic mean $\bar{x}$ ± mean absolute deviation) measured by TEM, AFM, ζ potential and yield of the hydrolysis as a function of the HCl exposure duration.

| Hydrolysis time	Length (nm)	Width (nm)	Aspect ratio	Height (nm)	ζ potential (mV)	Yield (%)
Control	2368 ± 3342	96 ± 128	22 ± 12	/	-29.1	98
30 min	803 ± 734	22 ± 13	31 ± 15	30 ± 14	-24.4	89
1 h	475 ± 380	21 ± 15	25 ± 14	26 ± 13	-29.6	90
2 h	247 ± 158	12 ± 5	23 ± 14	13 ± 7	-19.2	92
4 h	196 ± 131	13 ± 5	16 ± 8	15 ± 12	-9.8	90
8 h	144 ± 80	10 ± 4	16 ± 9	12 ± 9	-9.4	90

Crystallinity

Cellulose is often assessed in the light of X-ray diffraction. Yet, the analysis of the diffractograms is often simplified in the sense that the analyses are not based on a thorough physical model that would describe the state of the cellulosic matter. A first common method is the conventional peak fitting technique. This technique focuses on a small number of arbitrarily prominent peaks. Therefore, it largely ignores a large number of low to medium intensity diffraction rays. These rays are then mistakenly accounted for in the so-called amorphous background.(Thygesen et al. 2005; French and Santiago Cintrón 2012; Ahvenainen et al. 2016; Duchemin 2017b) Furthermore, the shape of the crystallites cannot be obtained using such a routine. The second method relies on the simulation of whole powder diffractograms using the Rietveld method.(De Figueiredo and Ferreira 2014; Ramírez and Bucio 2018) The Rietveld method is powerful, but it doesn't always implement an anisotropic line broadening routine that describes the size and shapes of non-spherical nanocrystals that display ample peak broadening and overlap. When it does, the implementation of the anisotropic size broadening is not necessarily well-adapted to the needle-like and convex shape of cellulose nanocrystallites. These issues are discussed in detail elsewhere.(Duchemin 2017b) In the present work, a parametric model is proposed in which the size and shape (assuming no microstrain contribution) of the native Iβ cellulose crystallites are modelled together and fitted to the experimental diffractograms. Five main parameters can be adjusted to provide simulated diffractograms of Iβ crystallites: three radii and two shape parameters, as described in the experimental section. Examples of simulated diffractograms and the corresponding crystallite shapes are illustrated in Figure 3. As expected, size and aspect ratio have a strong impact on the diffractograms (Figure 3a and b). It is also of specific interest to notice how the (110) and (1$\bar{1}$0) peaks are affected by the lateral shape (parameter *n*). Depending on *n*, the peaks can overlap or appear as two well separated Bragg rays (Figure 3c). The longitudinal shape parameter *m* influences the diffractogram in a subtler way by affecting the (102) ray and other reflections such as the (*h k* 3) reflections located above 2.θ = 30° (Figure 3d). These reflections are usually not analyzed when performing the analysis on powder patterns by curve fitting, demonstrating the potential use of this model if one wants to get the three-dimensional line-broadening information instead of the sole "cross-sectional" information contained in the three main diffraction bands (110), (1$\bar{1}$0) and (200). It is also possible to plot a discrete three-dimensional hull where each point is oriented perpendicular to a diffraction plane and at a distance from the origin equal to half the diameter of the crystallite in this direction (Figure S5).
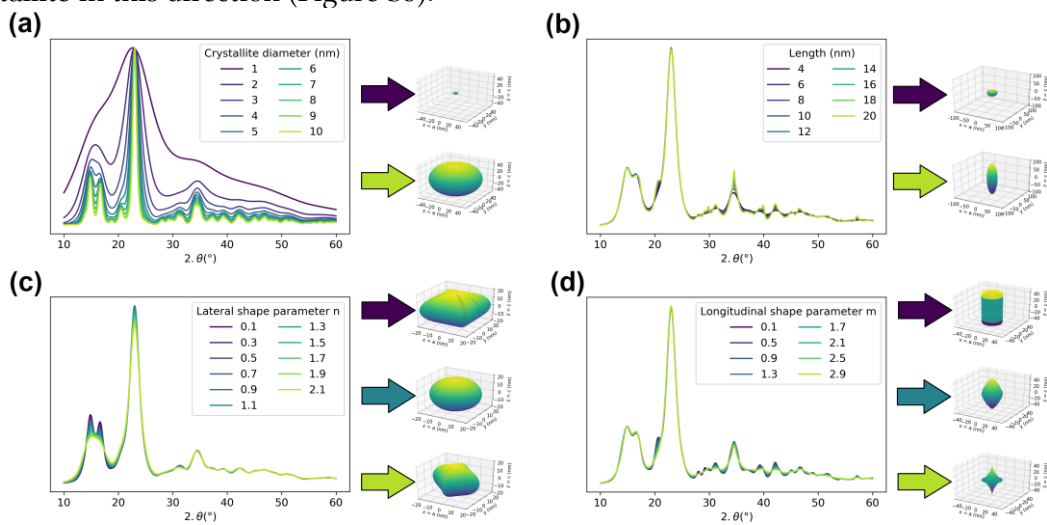
Figure 3. Simulated diffractograms of (a) isotropic Iβ crystallites with *m* = *n* = 1 and r_X = r_Y = r_Z, (b) elongated Iβ crystallites with *m* = *n* = 1 and r_X = r_Y = 2 nm, (c) laterally deformed Iβ crystallites with r_X = r_Y = r_Z = 2 nm and *m* = 1 and (d) longitudinally deformed Iβ crystallites with r_X = r_Y = 2 nm, r_Z = 5 nm and *n* = 1.

10
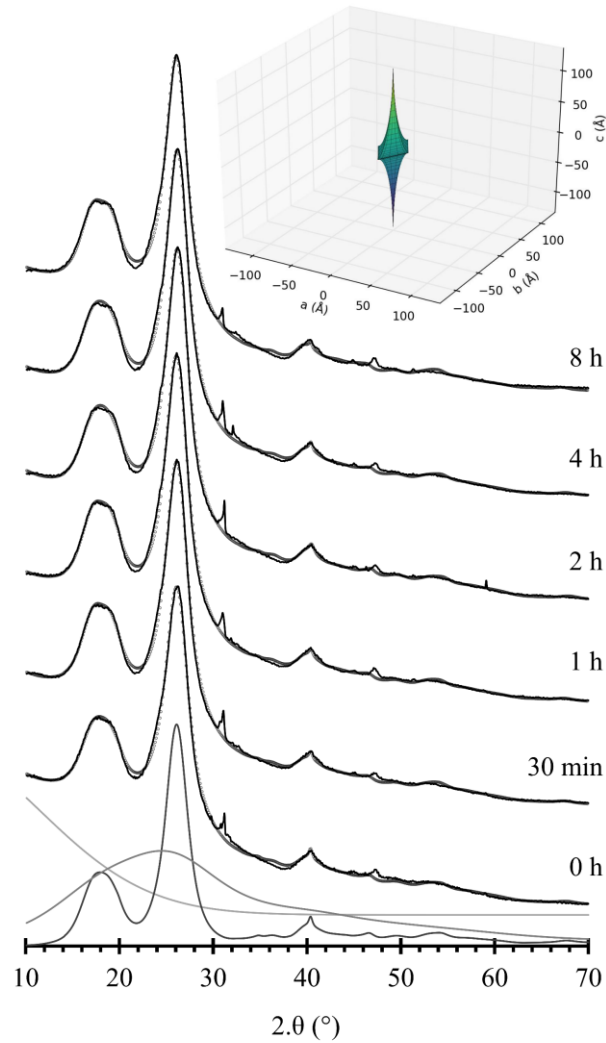
Figure 4. X-ray diffractograms (black lines) and simulated diffractograms (grey circles) after various hydrolysis times. The simulation of the control samples (0 h) is shown at the bottom with the background signal (light grey), the cellulose IV$_I$ signal (grey) and the cellulose I$_\beta$ signal (dark grey). An insert (top right) shows the crystallographic shape of the nanocrystals obtained after an 8 h long hydrolysis.

The model was then fitted to the experimental diffractograms of CNC produced in this work (Figure 4). The results show that the nanocrystals belong to the cellulose I family and remain fairly unaffected throughout the hydrolysis process in terms of shape (Table 2). The lateral shape of the crystallites was found to be that of a diamond ($1.84 < n < 2.25$), in accordance with the most common model currently employed for cellulose nanocrystals.(Viëtor et al. 2000; Nishiyama et al. 2012) Interestingly, the longitudinal shape was also that of an elongated and recessed bipyramid ($2.85 < m < 3.59$). This shape suggests either a straight dimensional cutoff (*i.e.* a finite length) or, alternatively, lattice periodicity discontinuities introduced by the presence of placement defects, vacancies, twinning, bending or twisting.(Hosemann et al. 1985; Nishiyama et al. 2012; Newman et al. 2013; Lindner et al. 2015) The helical twist hypothesis induces geometric frustrations along the microfibril axis and excess displacements of the outer chains with respect to the chains located at (or near) the helix axis.(Bruss and Grason 2012; Panaitescu et al. 2017) The lattice displacement induced by the twist grows larger from the center to the periphery, which is consistent with the size-broadening distribution measured here: all the (hkl) planes with $l \neq 0$ would be very sensitive to such a displacement. However, the cross-sectional dimensions of the crystallites as measured by XRD would be rather invariant and insensitive to the twist since the same amount of scatterers

11

is found throughout the cross-section by translation along the microfibril axis: this applies to the standard measurements performed on the (hk0) bands. If this the case, the current work would constitute the first "*in-situ*" evidence of crystallographic twist. In addition, the strains induced by the twist would also create very periodic crystallographic/topological defects (*i.e.* dislocations) under the continuum theory.(Azadi and Grason 2012; Panaitescu et al. 2017) For a given microfibril size (*i.e.* 18 chains, 36 chains, etc), these periodic defects could explain the LODP and the presence of I_α/I_β stacking faults. These defects acting as hydrolysis *loci* would also explain why the longitudinal shape measured here is insensitive to the hydrolysis.(Nyström et al. 2018)

The diameter of the crystallites in the direction orthogonal to the most intense (200) plane is ~$2.r_x \pm 7\%$ and the diameter in the direction orthogonal to the (010) plane is $2.r_y$. Hydrochloric acid hydrolysis induced a manifest increase of diameter (+22%) in the directions orthogonal to the (010) plane; this unidirectional thickening is attributed to a co-crystallization along the hydrophilic $\{110\}$, $\{1\bar{1}0\}$ and possibly $\{010\}$ planes (Table 2). It can be explained by a progressive adsorption of cellulose chains (co-crystallization) on the sides of the crystallites by creation of hydrogen bonds.(Newman 2004; Kontturi et al. 2016) These adsorbed chains are probably chain segments that were granted extra mobility by the chain scissions occurring during the hydrolysis. ^{13}C CP/MAS NMR showed that the samples that were not hydrolyzed displayed a C4 ratio consistent with 59% of the cellulose chains in the amorphous or exposed regions whereas the sample hydrolyzed for 8 h had a ratio of 55% (Figure S3). Both XRD and NMR results are therefore in good agreement with the slight co-crystallization observed in the initial report by Kontturi *et al.*(Kontturi et al. 2016)

As the crystallite length is $2r_z$, the longitudinal dimension of the nanocrystals was estimated to be in the 16.4 to 25.8 nm range and there was no statistical effect of the hydrolysis on this length.

The maximum lateral dimensions of the crystallites are 2-3 times less than that of the nanoparticles as discussed using TEM or AFM. Therefore, the nanoparticles produced by HCl hydrolysis are lateral aggregates of nanocrystals. Their crystallographic length is 6-40 times smaller than that measured by microscopy; at that stage possible explanations include long-range lattice displacements produced by bending and twisting, as detailed above.

There is still more information that can be extracted from the diffractograms. The stacking fault probability q could be estimated using the method proposed by Driemeier *et al.*(Driemeier and Francisco 2014) In this work, q amounted to no more than 20% (Table 2). The I_α/I_β ratio was also estimated using the C-1 signal of the ^{13}CP/MAS NMR experiment. It was found to be no more than 10% for the control sample and the sample hydrolyzed for 8 h, confirming (i) a good agreement between XRD and NMR and (ii) the large prevalence of the I_β allomorph in such vascular tissues. The crystallinity was also of interest. The crystallinity as assessed by XRD in this work was found to be invariant as variations in cellulose I, cellulose IV and background signal displayed no clear trend (Table 2). For the sake of discussion, the popular crystallinity index devised by Segal (1959) in his seminal work is also reported (Table 2).(Segal et al. 1959) Its value slightly increased after hydrolysis. As demonstrated in other works, this increase can here be attributed to a crystallite thickening without necessarily involving a change in the amorphous/crystalline ratio *stricto sensu*.(Duchemin et al. 2007; French and Santiago Cintrón 2012) The paracrystalline cellulose IV_I modelled in this work was isotropic with a size of 7.4-8 Å, meaning domains no more than 2-3 glucose monomers packed side-by-side. These domains produce a Bragg scatter with a well-defined interplanar distance. They are thus relatively ordered, supporting the hypothesis of a biphasic model comprising comparatively large "bi-pyramidal coherent" I_β crystallites and small IV_I stacks. It seems to indicate that elementary fibrils in the native state are in fact aggregates of crystallites and tightly packed small paracrystalline domains acting as anchor knots (interconnections)

between the crystallites. The presence of amorphous material *stricto sensu* in the form of individual and randomly oriented chains was not accounted for in the present model. However, the data could be described with a good level of accuracy, which means that only minor amounts of such amorphous material, if any, could be present.

Other nanocrystals produced by sulfuric acid or ammonium persulfate hydrolysis run in our laboratory comprise almost no cellulose IV_I domains (data not shown here). This point is of particular interest since the HCl vapor method produces nanoparticles with no surface charges and with a minimum amount of mass loss.

Table 2. Results of the simulation of X-ray diffractograms using a Rietveld analysis routine with a superellipsoid model to describe the three-dimensional shape of the cellulose nanocrystals.

Hydrolysis time	Control	30 min	1 h	2 h	4 h	8 h
Segal's *CrI* (%)(Segal et al. 1959)	53%	55%	56%	57%	57%	56%
Lattice parameter *a* (Å)	7.96	7.96	7.97	7.94	7.94	7.98
Lattice parameter *b* (Å)	8.17	8.18	8.18	8.15	8.17	8.22
Lattice parameter *c* (Å)	10.36	10.36	10.36	10.34	10.36	10.37
γ (°)	95.53	95.75	95.73	95.31	95.52	95.82
March-Dollase strength	1.40	1.52	1.54	1.38	1.54	1.65
r_x (Å)	18	18	18	19	19	19
r_y (Å)	27	28	29	27	30	33
r_z (Å)	113	114	102	82	129	129
Superellispoid longitudinal squareness *m*	3.44	3.59	3.36	2.85	3.46	3.33
Superellispoid radial squareness *n*	2.02	1.84	1.87	2.25	2.26	2.01
Cellulose IV_I size (Å)	7.4	7.8	7.8	7.3	7.6	8.0
Background (%)	42%	42%	42%	38%	41%	44%
I_β (%)	22%	23%	23%	25%	23%	21%
IV_I (%)	36%	35%	35%	37%	36%	35%
Stacking fault probability *q* (%)	10	10	10	20	10	10
Correlation coefficient	0.99896	0.99915	0.99913	0.99905	0.99899	0.99901
R-pattern	1.97%	1.76%	1.83%	1.86%	1.90%	2.05%

Temperature-dependent ATR-FTIR
In this work, the control material as well as the hydrolyzed material (8 h) were studied. Both materials were either used (i) "as is", in their protonated form, (ii) labelled by deuterium exchange and (iii) back-exhanged and thoroughly dried in order to assess the amount of *drying* hysteresis. The ATR-FTIR experiment was conducted from 20°C to 260°C (Figure 4), and the samples were then cooled down to look at possible *thermal* hysteretic effects and phase changes.

Background
Replacing H_2O with D_2O in a cellulose suspension *at room temperature* leads to a limited isotopic exchange. In contrast, the use of high temperatures or swelling agents can lead to a complete replacement of hydrogen by deuterium.(Sepall and Mason 1961; Nishiyama et al. 1999) Such harsh conditions will not be discussed in the present work. It is particularly

informative to monitor the isotopic exchange by FTIR spectroscopy because the exchanged -OD groups will have an elongational vibration ν_{OD} near 2500 cm^{-1} instead of 3600-3200 cm^{-1} for ν_{OH}. Therefore, the −OD signal can easily be distinguished from the −OH one. The −OH signal is a superimposition of several bands. In general, it is agreed that the small band at 3650-3600 cm^{-1} is attributed to unbound water molecules.(Fengel 1993; Kondo and Sawatari 1996; Olsson and Salmén 2004) Bands at 3580 and 3555 cm^{-1} were assigned to loosely bond water or perhaps to non-hydrogen bonded O(2)H and O(6)H groups in amorphous cellulose.(Kondo and Sawatari 1996; Michell and Higgins 1999; Olsson and Salmén 2004; Hofstetter et al. 2006; Watanabe et al. 2006a) Regarding cellulose I$_\beta$, there is a general agreement on the following band assignment: an intramolecular O(2)H···O(6) band at 3460-3436 cm^{-1}, an intermolecular O(6)H···O'(3) at 3412 cm^{-1}, an intramolecular O(3)H···O(5) band at 3340-3360 cm^{-1}, an intramolecular O(2)H···O(6) band at 3270 cm^{-1} and an intermolecular O(3)H···O'(6) band at 3230 cm^{-1}.(Marechal and Chanzy 2000; Hofstetter et al. 2006; Watanabe et al. 2006a; Hayakawa et al. 2017) Recently, it was demonstrated by CPMD calculation that the vibrations at 3340 and 3270 cm^{-1} were resolved and could be assigned without ambiguity.(Hayakawa et al. 2017) However, the complexity of the band perpendicular to the chain direction and with peaks at 3410, 3345 and 3305 cm^{-1} was explained by variations in elongational frequencies between the −OH groups found in the origin and center chains. In contrast, the −OD signal obtained on surface deuterated samples only shows one broad ν_{OD} band near 2500 cm^{-1}. The presence of a single broad band that is not further resolved by polarization, suggests the presence of unstructured −OD groups.(Priest and Shimell 1963; Hofstetter et al. 2006; Driemeier et al. 2015) This result is confirmed by inelastic neutron scattering.(Müller et al. 2000) Both cellulose I and cellulose IV$_I$ contain similar well-identified ν_{OH} bands in the 3800-3000 cm^{-1} area of the spectrum, reinforcing the assumption that cellulose IV$_I$ is just a form of small and imperfect I$_\beta$ crystallites, as already inferred in the XRD analysis conducted in this work.(Marrinan and Mann 1956; O'Connor et al. 1958)

A "soft" room temperature H_2O-D_2O isotopic exchange was used in numerous works to evaluate the water accessibility of different cellulose substrates.(Priest and Shimell 1963; Rousselle and Nelson 1971; Reishofer and Spirk 2015; Lindh and Salmén 2016) Only accessible hydroxyl groups are then prone to deuterium exchange, meaning that the hydroxyl groups located on the cellulose chains localized at the interior of the crystallites are essentially left unaffected.(Priest and Shimell 1963; Marechal and Chanzy 2000; Reishofer and Spirk 2015; Lindh and Salmén 2016) Consequently, the corresponding OD groups labelled by the exchange establish no hydrogen bonds with their surroundings.(Marechal and Chanzy 2000) Sometimes, the exchange or back-exchange procedure involves a certain amount of drying, which can lead to deuterium trapping due to hornification (co-crystallization).(Mann and Marrinan 1956a; Priest and Shimell 1963; Wadehra and Manley 1965; Rousselle and Nelson 1971; Suchy et al. 2010; Lemke et al. 2012; Agarwal et al. 2016; Lindh and Salmén 2016) These possible artefacts were anticipated as early as 1962 by Rousselle and Nelson who devised a method to assess the accessibility of cellulose by an isotopic back-exchange procedure in the wet state, without any drying.(Rousselle and Nelson 1971)

The effect of temperature on the molecular structure of cellulose has also been studied by FTIR spectroscopy.(Marechal and Chanzy 2000; Kokot et al. 2002; Wada 2002; Watanabe et al. 2006c, b) In general, the band positions are affected much more by temperatures above 100°C than they are by humidity variations.(Watanabe et al. 2006a) These studies were mainly focused on the hydroxyl group regions and demonstrated a good stability of the intramolecular O(2)H···O(6) bond. In contrast, a progressive change of the O(3)H···O(5) above 130 °C with a marked transition near 184°C-220°C was observed and assigned to a glass transition.(Kokot et al. 2002; Watanabe et al. 2006c) This transition is linked to the so-called "high-temperature form" of cellulose I$_\beta$ which has been evidenced by non-linearities in the lateral unit cell dimensions above 180°C of both *Cladophora* nanocrystals and tension wood.(Hori and Wada 2005; Wada et al. 2010) The formation of carbonyl groups above 220°C has also been observed

and attributed to dehydration reactions, *i.e.* thermal degradation of the glucosidic backbone.(Pastorova et al. 1994; Nam et al. 2020) The monitoring of this band, however, has never been performed *in-situ.*
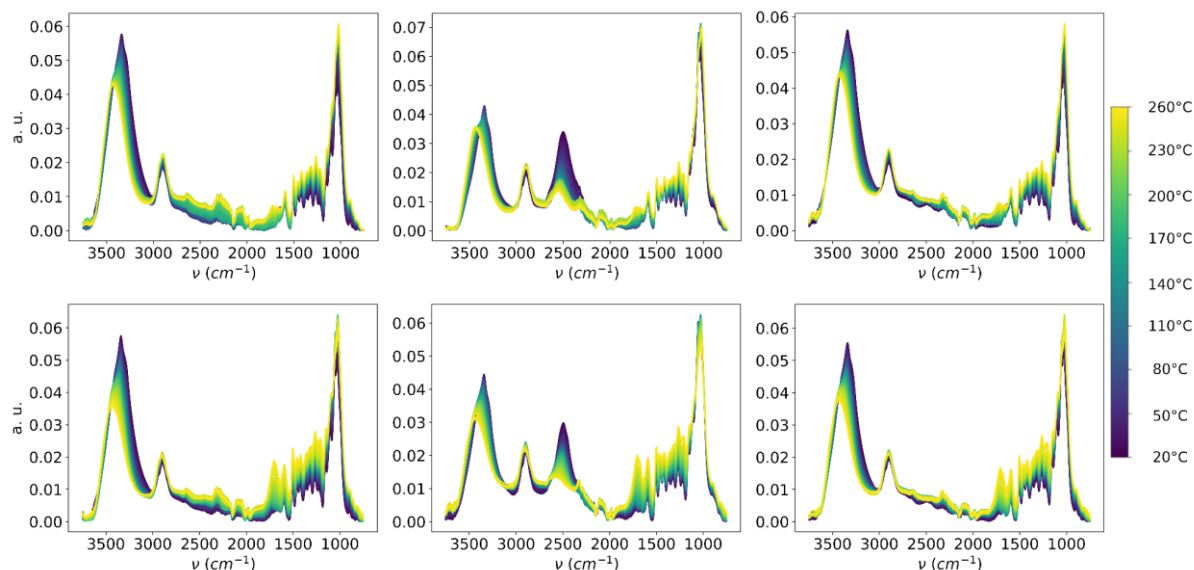
Figure 5. Absorbance FTIR spectra of the control sample (top row) and 8 h hydrolyzed sample (bottom row) as obtained after the deuterium-free control process (first column), after isotopic labelling with D_2O (second column) and after an isotopic labelling, drying, and hydrogen re-exchange (third column). The measurements were performed between room temperature and 260°C.

Effect of heating on hydration

The FTIR spectra show drastic changes in the ν_{OH} region with ample band shifts as seen directly (Figure 5), by peak maximum measurement (Figure S7) or by second derivative analysis (Figure S8). In contrast to the ν_{OH} results, the ν_{OD} region is less affected and the broad ν_{OD} band is only moderately shifted in frequency (Figure S7). The most prominent ν_{OD} shift occurs below *ca.* 100°C, which is concomitant with the drying (Figures 5 and S7). When compared to the ν_{OH} intensity, the ν_{OD} intensity is largely reduced by the temperature sweep. It is of particular interest to calculate the ratio r_{access} of deuterium exchanged hydroxyl groups and bound water over the total amount of non-exchanged hydroxyl groups (Figure 6a). This was done with equation (6). In the present experimental setup, r_{access} *could* decrease due to combined dehydration and back-exchange. The dehydration occurred due to heating. The back-exchange was triggered by the moisture of the air surrounding the sample that enables deuterium-hydrogen exchanges. However, comparisons between the samples are still of interest. In particular, the initial values were not affected by possible back-exchange because the measurements were performed immediately after opening the air-tight container with the labelled samples. This r_{access} calculation shows that the non-hydrolyzed sample initially contained about 47% of labelled deuteroxyl groups on cellulose and D_2O against 38% for the sample that was hydrolyzed. This initial ratio ranking is counterintuitive because the hydrolyzed sample is expected to have a higher surface to volume ratio and similar crystallinity (XRD results) when compared to the non-hydrolyzed material. Therefore, this difference at low-temperature doesn't originate from a larger amount of hygroscopic amorphous regions in the hydrolyzed material. Bound water might then be an explanation. A higher water content is indeed confirmed by the intensity of the band at 1640 cm^{-1} (Figures 7 and S13). The samples were expected to contain only bound water since they were dried with dry N_2 before being equilibrated for a week with H_2O or D_2O under the water saturation point

15

for cellulose. Bound water could be trapped in pores or defects. These pores or defects are probably opened or suppressed during the production of nanoparticles, explaining the initial differences in D_2O content and also the absence of trapped D_2O in the nanoparticles after the H_2O back-exchange procedure (Figure 6b).(Strømme et al. 2003)

When the samples were heated, both r_{access} ratios decreased with temperature (Figure 6). The decrease was initially much faster for the non-hydrolyzed sample. The two curves crossed each other near 100°C and then stabilized with a fairly linear behavior all the way from 100°C to 260°C, confirming moisture evaporation in a process also involving polymer dehydration and dynamic reprotonation. On this high temperature range, r_{access} was always higher for the nanoparticles, as expected given their higher surface to volume ratio. Water evaporation was confirmed by plotting the intensity of the band at 1640 cm^{-1} against temperature (Figure 7). This plot shows a signal decreasing in intensity from 20°C to ~100° for the non-hydrolyzed sample and to ~120°C for the hydrolyzed sample. As opposed to the r_{access} data, the intensity of the band remains lower for the hydrolyzed sample up to the onset of cellulose dehydration near 180°C, in accordance with a lower water content.

Therefore, the deuterium exchange procedure should be used with care when assessing cellulose crystallinity or "accessibility" since the intrinsic hygroscopic moisture content of the substrate can introduce an important bias in the measurement. This moisture content can be largely affected by the transient porosity and it doesn't necessarily depend on the crystallinity. This bias is minimized above ~100°C and high temperature FTIR brings a critical information to deuterium labelling experiments.
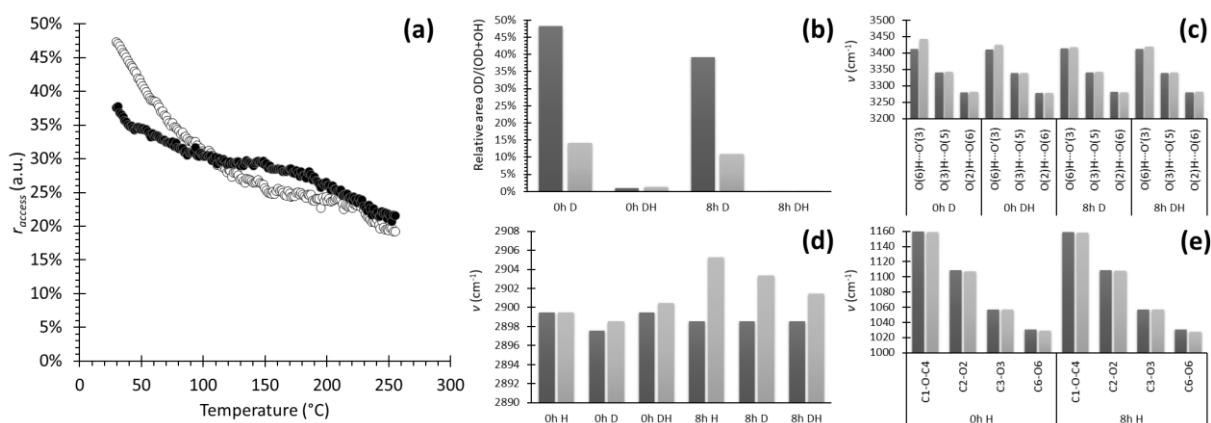
Figure 6. (a) Relative areas of the ν_{OD} region expressed as r_{access} for the non-hydrolyzed sample (○) and the sample that was hydrolyzed for 8 h (●). Comparisons of various parameters at room temperature before (dark grey) and after (light grey) the completion of the heating cycle for the normally protonated samples (H), the deuterated samples (D) and the samples that were deuterated and then reprotonated (DH). These parameters are (b) the relative deuterated fraction, (c) the position of the main inter- and intramolecular bands in the ν_{OH} region, (d) the maximum of the band in ν_{CH} region and (e) the positions of the three main C-O bonds found in cellulose chains.
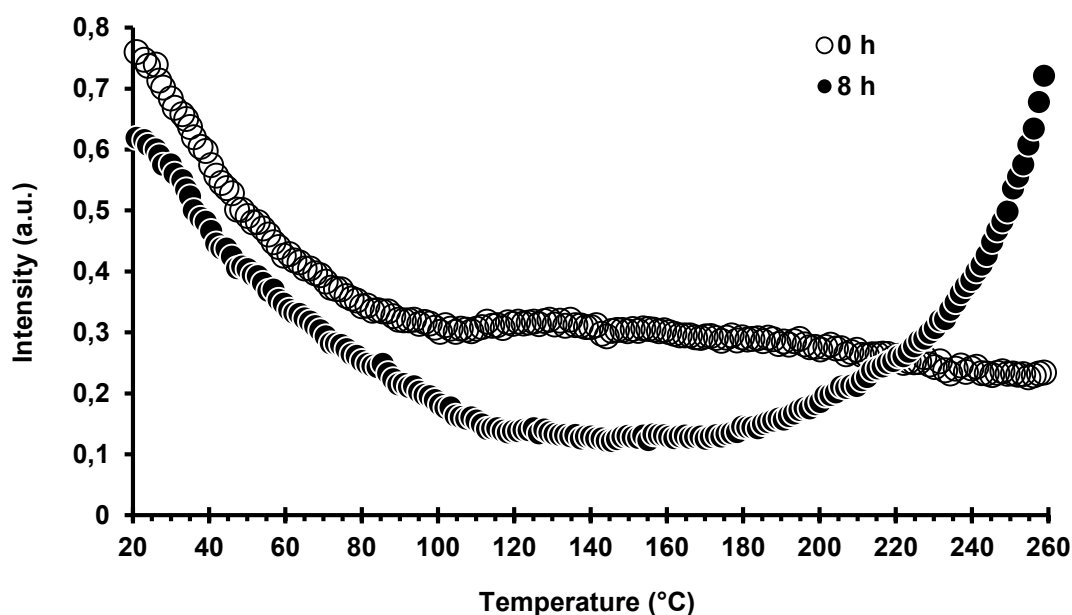
Figure 7. Intensity of the molecular water maxima near 1640 cm^{-1} as a function of the temperature for the sample that was not hydrolyzed (○) and the sample that was hydrolyzed for 8 h (●). The signals were normalized with respect to intensity of the −CH band near 2900 cm^{-1}. The intensity increase observed after 180°C for the hydrolyzed sample is attributed to the onset of cellulose dehydration (see Figures 7 and S12).

Effect of heating on specific bonds

It is explanatory to look at the ν_{OH} region in more detail. The plot of the second derivative shows a linear shift of the three main peaks (Figure S8). The maxima of the second derivative plots were sharp for the intermolecular O(6)H···O'(3) band at ~3410 cm^{-1}, the intramolecular O(3)H···O(5) band at ~3340 cm^{-1} and the other intramolecular O(2)H···O(6) band at ~3280 cm^{-1} (band frequencies at room temperature). The positions of the maxima were used to assess the amplitudes of the three bands at all temperatures (Figure S9).

It can be seen that the intensities of the intermolecular O(6)H···O'(3) become more intense during heating between 100°C and *ca.* 200°C, whereas both the intramolecular O(3)H···O(5) and O(2)H···O(6) intensities decrease. The hydrolysis has not marked effect on these bonds in this temperature range. This is a strong indication of a redistribution of the hydrogen bond network upon dehydration, with cellulose-water bonds supposedly replaced by cellulose-cellulose bonds. The acid hydrolysis has however a marked effect above *ca.* 230°C: the intensities of all the bonds undergo a sharp decrease between 230°C and 260°C on the hydrolyzed material only (Figure 5 and S9). This intensity drop is concomitant with a disruption of the whole hydrogen bond network. The explanation cannot come from a crystallinity difference, as evidenced by X-ray diffraction. Therefore, this transition can be attributed to cellulose thermal degradation or thermal motion. Thermal degradation is known to be triggered by the cellulose reducing ends and the higher number of reducing ends after hydrolysis can explain the difference between the two materials.(Matsuoka et al. 2011; Agustin et al. 2016) During this degradation, intra-ring condensation and rearrangements lead to the formation of furans and phenols in place of anhydroglucose units in the cellulose chain.(Pastorova et al. 1994; Nam et al. 2020) This mutation forms carbonyl groups. In this work, the hydrolyzed material was found much more sensitive than the non-hydrolyzed material to this temperature degradation: in particular, a strong carbonyl C=O band near 1702 cm^{-1} was formed between 180 and 200°C and its intensity increased abruptly up to 260°C during the heating cycle (Figures 5, 8a and S12), confirming chemical degradation. The

evolution of the band at 1590 cm^{-1} (aromatic skeletal vibration of lignin) could be attributed to lignin polycondensation in the course of the thermal cycle.

These thermo-chemical transformations also correspond to the two $\alpha_{2,2}$ and $\alpha_{2,1}$ viscoelastic relaxations of cellulose I and the creation of high-temperature cellulose I$_\beta$.(Kokot et al. 2002; Hori and Wada 2005; Watanabe et al. 2006c; Wada et al. 2010; Duchemin et al. 2014) Therefore, the thermally induced reorganization of the hydrogen bond network can also be considered as a thermal process during which chain segments gain extra mobility. Shorter segments produced by hydrolysis ease thermal mobility.

(a)

(b)
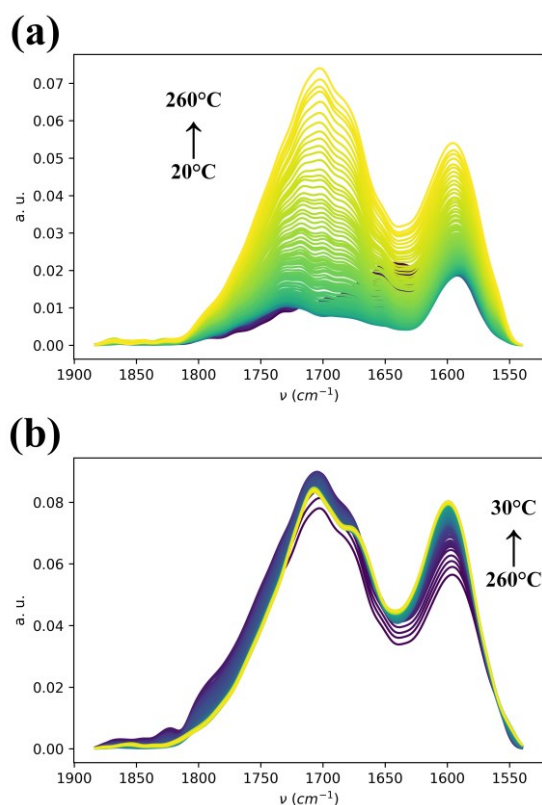
Figure 8. Evolution of the carbonyl signal on the absorbance spectra during (a) heating from 20°C (blue) to 260°C (yellow) and (b) cooling from 260°C (blue) to 30°C (yellow) of the non-deuterated sample hydrolyzed for 8 h.

Hysteretic effects

The spectra were compared at room temperature before and after completion of the heating cycle as performed during the ATR-FTIR scan. The hydrolysis had nearly no effect on the positions of the hydrogen bonds (Figure 6c). However, the heating cycle markedly displaced the intermolecular O(6)H···O'(3) which can be attributed to both an evaporation of bound water and chain degradation. This evaporation also induced a distortion of the hydrogen bond network resulting in hornification or co-crystallisation. Interestingly, the two intramolecular bonds were poorly affected by this process, which is an indication that the distortion is structural (long-range aggregation). This result also means that the high temperature collapse of the hydrogen bond network undergone in the hydrolyzed sample (Figure S9) is reversible to a large extent.

The positions of the maxima of the –CH band near 2900 cm^{-1} were significantly affected by the heat cycle and shifted by ~5 cm^{-1} after the samples were hydrolyzed (Figure 6d). This displacement is concomitant with a thermal degradation favored by reducing chain ends, as detailed above. The intense carbonyl band appearing during heating in the hydrolyzed material remains stable after cooling (Figure 8b), as observed in other works.(Pastorova et al. 1994; Nam et al. 2020)

Furthermore, the dismantlement of the cellulose system into smaller nanofragments granted extra longitudinal and lateral mobility to the cellulose chains for reorganization during heating and dehydration, as seen above.(Matsuoka et al. 2014; Nam et al. 2020) This could explain the shift of the −CH band, a band that is otherwise known to be sensitive to the crystallinity of the material.(Marrinan and Mann 1956; Schwanninger et al. 2004; Ciolacu et al. 2011) Regarding the C-O intrachain bonds as measured using the positions of the C-O stretching region, small hysteretic variations can be observed (Figure 6e and S11) but the cellulosic backbone remained essentially unaffected.(Marechal and Chanzy 2000; Watanabe et al. 2006b) For all the samples, the least affected bond was C3-O3 (Δ_{0h} and Δ_{8h} = 0 cm^{-1}) and the most affected bonds were C2-O2 (Δ_{0h} = -2 cm^{-1} and Δ_{8h} = -1 cm^{-1}) and especially C6-O6 (Δ_{0h} = -2 cm^{-1} and Δ_{8h} = -3 cm^{-1}). The glycosidic C1-O-C4 bond was affected in an intermediary way (Δ_{0h} and Δ_{8h} = -1 cm^{-1}). The C3-O3 relative "inertness" is certainly due its in-plane conformation and to its orientation running parallel to the C1-O-C4 bond, along the chain axis. The singularity of the C6-O6 band is most certainly linked to its central role in the hydrogen bond network. This singular band shift can be explained by the higher sensitivity of the hydrogen bond network to temperature-induced deformations when the polymer chain fringe structure is dismantled and when the long-range polymer constrains are alleviated, *i.e.* when the longitudinal chain connectivity is lost due to chain scission.

Conclusions

Hydrochloric acid hydrolysis in the vapor phase offers a unique opportunity to open up the cellulose structure without affecting the crystallinity and with almost no monomer production when compared with the popular sulfuric acid hydrolysis.(Kontturi et al. 2016) In the present work, a cellulose source from vascular flax bundles was bleached and submitted to such an acid hydrolysis. A three-dimensional X-ray diffraction Rietveld analysis showed that the crystallinity changes were not significant whereas the lateral size variations were substantial, in the order of 22% on the hydrophilic surfaces. The crystallographic model measures a certain paracrystalline content consisting of stacks containing 2 or 3 monomers arranged in a periodic manner. In that sense, the hypothesis of cellulose microfibrils being fractal aggregates of 3 × 2 chains, in accordance with the current knowledge on hexameric terminal complexes, is plausible.(Usov et al. 2015) This paracrystalline content is not affected in size or relative content by the hydrolysis. This result suggests that the HCl hydrolysis does not proceed by full hydrolysis of the least ordered regions, unlike H$_2$SO$_4$ hydrolysis, which explains the high yield of the method. This result is compatible a progression of the HCl hydrolysis through accessible regions or kinks.(Nyström et al. 2018)

Isotopic labelling with D$_2$O and thermal ATR-FTIR results demonstrated that temperatures above 100℃ can be used to reveal the higher amount of labelled sites in the hydrolyzed material when the material is conditioned at 75 % RH. This result also means that hygroscopic moisture can induce an important bias in the quantitative assessment of accessibility (or "crystallinity") by deuterium labelling. In this work, two materials with very close crystallinities but with different morphologies (fibres and nanoparticles) had very different accessibilities, meaning that deuterium labelling cannot measure crystallinity. Thermal ATR-FTIR also evidenced small hysteretic effects of the hydrogen bond network and cellulose backbone (C-O stretching region) to temperature variations after hydrolysis. The effect is more prevalent for all interatomic linkages relative to the hydroxymethyl group (C6). The irreversible formation of a carboxylic band at 1702 cm^{-1} is characteristic of the cellulose degradation by dehydration reactions.

Finally, the nanoparticles produced in this work were stable aggregates regarding the effect of wetting and drying cycles (deuterium trapping was cancelled by the hydrolysis). However, their polymer chains were more susceptible to thermal motion and degradation

above *ca.* 200°C was evidenced by the rise of the carbonyl group signal. These two effects should be attributed to the topology of the cellulosic substrate (chain ends, chain entanglement, adjacency, chain continuity between highly ordered regions) rather than to their crystallinity, as measured by XRD.

Supporting information:
The analysis of the bleaching steps, the ^{13}C CP/MAS NMR spectra, additional ATR-FTIR spectroscopy data treatment are provided as supplementary information, after the references.

REFERENCES:
Agarwal UP, Ralph SA, Reiner RS, Baez C (2016) Probing crystallinity of never-dried wood cellulose with Raman spectroscopy. Cellulose 23:125–144. https://doi.org/10.1007/s10570-015-0788-7

Agustin MB, Nakatsubo F, Yano H (2016) The thermal stability of nanocellulose and its acetates with different degree of polymerization. Cellulose 23:451–464. https://doi.org/10.1007/s10570-015-0813-x

Ahvenainen P, Kontro I, Svedström K (2016) Comparison of sample crystallinity determination methods by X-ray diffraction for challenging cellulose I materials. Cellulose 23:1073–1086. https://doi.org/10.1007/s10570-016-0881-6

Araki J, Wada M, Kuga S, Okano T (1998) Flow properties of microcrystalline cellulose suspension prepared by acid treatment of native cellulose. Colloids Surf Physicochem Eng Asp 142:75–82. https://doi.org/10.1016/S0927-7757(98)00404-X

Azadi A, Grason GM (2012) Defects in crystalline packings of twisted filament bundles. II. Dislocations and grain boundaries. Phys Rev E 85:031604. https://doi.org/10.1103/PhysRevE.85.031604

Battista OA, Coppick S, Howsmon JA, et al (1956) Level-Off Degree of Polymerization. Ind Eng Chem 48:333–335. https://doi.org/10.1021/ie50554a046

Beisl S, Miltner A, Friedl A (2017) Lignin from micro-to nanosize: production methods. Int J Mol Sci 18:1244

Bondeson D, Mathew A, Oksman K (2006) Optimization of the isolation of nanocrystals from microcrystalline cellulose by acid hydrolysis. Cellulose 13:171–180. https://doi.org/10.1007/s10570-006-9061-4

Bruss IR, Grason GM (2012) Non-Euclidean geometry of twisted filament bundle packing. Proc Natl Acad Sci 109:10781–10786. https://doi.org/10.1073/pnas.1205606109

Calvini P (2005) The influence of levelling-off degree of polymerisation on the kinetics of cellulose degradation. Cellulose 12:445–447

Calvini P, Gorassini A, Merlani AL (2007) On the kinetics of cellulose degradation: looking beyond the pseudo zero order rate equation. Cellulose 15:193. https://doi.org/10.1007/s10570-007-9162-8

Camarero Espinosa S, Kuhnt T, Foster EJ, Weder C (2013) Isolation of Thermally Stable Cellulose Nanocrystals by Phosphoric Acid Hydrolysis. Biomacromolecules 14:1223–1230. https://doi.org/10.1021/bm400219u

Ciolacu D, Ciolacu F, Popa VI (2011) Amorphous cellulose—structure and characterization. Cellul Chem Technol 45:13

De Figueiredo LP, Ferreira FF (2014) The Rietveld Method as a Tool to Quantify the Amorphous Amount of Microcrystalline Cellulose. J Pharm Sci 103:1394–1399. https://doi.org/10.1002/jps.23909

Demšar J, Curk T, Erjavec A, et al (2013) Orange: data mining toolbox in Python. J Mach Learn Res 14:2349–2353

Dong S, Bortner MJ, Roman M (2016) Analysis of the sulfuric acid hydrolysis of wood pulp for cellulose nanocrystal production: A central composite design study. Ind Crops Prod 93:76–87. https://doi.org/10.1016/j.indcrop.2016.01.048

Driemeier C, Francisco LH (2014) X-ray diffraction from faulted cellulose I constructed with mixed Iα–Iβ stacking. Cellulose 21:3161–3169. https://doi.org/10.1007/s10570-014-0390-4

Driemeier C, Mendes FM, Ling LY (2015) Hydrated fractions of cellulosics probed by infrared spectroscopy coupled with dynamics of deuterium exchange. Carbohydr Polym 127:152–159. https://doi.org/10.1016/j.carbpol.2015.03.068

Du H, Liu C, Mu X, et al (2016) Preparation and characterization of thermally stable cellulose nanocrystals via a sustainable approach of FeCl3-catalyzed formic acid hydrolysis. Cellulose 23:2389–2407. https://doi.org/10.1007/s10570-016-0963-5

Duchemin B (2017a) Anisotropic size-broadening and X-ray diffraction of cellulose Iβ: a route towards crystallite shape and crystallinity determination from powder patterns. Nantes, France

Duchemin B (2017b) Size, shape, orientation and crystallinity of cellulose Iβ by X-ray powder diffraction using a free spreadsheet program. Cellulose 1–15. https://doi.org/10.1007/s10570-017-1318-6

Duchemin B, Newman R, Staiger M (2007) Phase transformations in microcrystalline cellulose due to partial dissolution. Cellulose 14:311–320

Duchemin BJC, Staiger MP, Newman RH (2014) High-Temperature Viscoelastic Relaxation in All-Cellulose Composites. Macromol Symp 340:52–58. https://doi.org/10.1002/masy.201300123

Dufresne A (2013) Nanocellulose: From Nature to High Performance Tailored Materials. Walter de Gruyter

Eichhorn SJ, Dufresne A, Aranguren M, et al (2010) Review: current international research into cellulose nanofibres and nanocomposites. J Mater Sci 45:1. https://doi.org/10.1007/s10853-009-3874-0

Fang W, Arola S, Malho J-M, et al (2016) Noncovalent Dispersion and Functionalization of Cellulose Nanocrystals with Proteins and Polysaccharides. Biomacromolecules 17:1458–1465. https://doi.org/10.1021/acs.biomac.6b00067

Fengel D (1993) Influence of water on the OH valency range in deconvoluted FTIR spectra of cellulose. Holzforsch-Int J Biol Chem Phys Technol Wood 47:103–108

French AD, Santiago Cintrón M (2012) Cellulose polymorphy, crystallite size, and the Segal Crystallinity Index. Cellulose 20:583–588. https://doi.org/10.1007/s10570-012-9833-y

Guinier A (1963) X-ray diffraction in crystals, imperfect crystals, and amorphous bodies. W. H. Freeman and Company, San Francisco and London

Habibi Y, Lucia LA, Rojas OJ (2010) Cellulose Nanocrystals: Chemistry, Self-Assembly, and Applications. Chem Rev 110:3479–3500. https://doi.org/10.1021/cr900339w

Hayakawa D, Nishiyama Y, Mazeau K, Ueda K (2017) Evaluation of hydrogen bond networks in cellulose Iβ and II crystals using density functional theory and Car−Parrinello molecular dynamics. Carbohydr Res 449:103–113. https://doi.org/10.1016/j.carres.2017.07.001

Hofstetter K, Hinterstoisser B, Salmén L (2006) Moisture uptake in native cellulose – the roles of different hydrogen bonds: a dynamic FT-IR study using Deuterium exchange. Cellulose 13:131–145. https://doi.org/10.1007/s10570-006-9055-2

Hori R, Wada M (2005) The Thermal Expansion of Wood Cellulose Crystals. Cellulose 12:479. https://doi.org/10.1007/s10570-005-5967-5

Horikawa Y, Clair B, Sugiyama J (2009) Varietal difference in cellulose microfibril dimensions observed by infrared spectroscopy. Cellulose 16:1–8. https://doi.org/10.1007/s10570-008-9252-2

Hosemann R, Hentschel MP, Baltacalleja FJ, et al (1985) The Alpha-Star-Constant, Equilibrium State and Bearing Net Planes in Polymers, Bio-Polymers and Catalysts. J Phys C-Solid State Phys 18:961–971

Janoschek R, Hayd A, G. Weidemann E, et al (1978) Calculated and observed isotope effects with easily polarizable hydrogen and deuterium bonds. J Chem Soc Faraday Trans 2 Mol Chem Phys 74:1238–1245. https://doi.org/10.1039/F29787401238

Klemm D, Kramer F, Moritz S, et al (2011) Nanocelluloses: A New Family of Nature-Based Materials. Angew Chem Int Ed 50:5438–5466. https://doi.org/10.1002/anie.201001273

Kokot S, Czarnik-Matusewicz B, Ozaki Y (2002) Two-dimensional correlation spectroscopy and principal component analysis studies of temperature-dependent IR spectra of cotton-cellulose. Biopolymers 67:456–469. https://doi.org/10.1002/bip.10163

Kondo T, Sawatari C (1996) A fourier transform infra-red spectroscopic analysis of the character of hydrogen bonds in amorphous cellulose. Polymer 37:393–399

Kontturi E, Meriluoto A, Penttilä PA, et al (2016) Degradation and Crystallization of Cellulose in Hydrogen Chloride Vapor for High-Yield Isolation of Cellulose Nanocrystals. Angew Chem Int Ed 55:14455–14458. https://doi.org/10.1002/anie.201606626

Lam E, Male KB, Chong JH, et al (2012) Applications of functionalized and nanoparticle-modified nanocrystalline cellulose. Trends Biotechnol 30:283–90. https://doi.org/10.1016/j.tibtech.2012.02.001

Lemke C, Dong R, Michal C, Hamad W (2012) New insights into nano-crystalline cellulose structure and morphology based on solid-state NMR. Cellulose 19:1619–1629. https://doi.org/10.1007/s10570-012-9759-4

Leung ACW, Hrapovic S, Lam E, et al (2011) Characteristics and Properties of Carboxylated Cellulose Nanocrystals Prepared from a Novel One-Step Procedure. Small 7:302–305. https://doi.org/10.1002/smll.201001715

Li B, Xu W, Kronlund D, et al (2015) Cellulose nanocrystals prepared via formic acid hydrolysis followed by TEMPO-mediated oxidation. Carbohydr Polym 133:605–612. https://doi.org/10.1016/j.carbpol.2015.07.033

Lin N, Huang J, Dufresne A (2012) Preparation, properties and applications of polysaccharide nanocrystals in advanced functional nanomaterials: a review. Nanoscale 4:3274–3294. https://doi.org/10.1039/C2NR30260H

Lindh EL, Salmén L (2016) Surface accessibility of cellulose fibrils studied by hydrogen–deuterium exchange with water. Cellulose 1–13. https://doi.org/10.1007/s10570-016-1122-8

Lindner B, Petridis L, Langan P, Smith JC (2015) Determination of cellulose crystallinity from powder diffraction diagrams. Biopolymers 103:67–73. https://doi.org/10.1002/bip.22555

Liu Y, Wang H, Yu G, et al (2014) A novel approach for the preparation of nanocrystalline cellulose by using phosphotungstic acid. Carbohydr Polym 110:415–422. https://doi.org/10.1016/j.carbpol.2014.04.040

Lorenz M, Sattler S, Reza M, et al (2017) Cellulose nanocrystals by acid vapour: towards more effortless isolation of cellulose nanocrystals. Faraday Discuss 202:315–330. https://doi.org/10.1039/C7FD00053G

Lourdin D, Peixinho J, Bréard J, et al (2016) Concentration driven cocrystallisation and percolation in all-cellulose nanocomposites. Cellulose 23:529–543. https://doi.org/10.1007/s10570-015-0805-x

Mann J, Marrinan HJ (1956a) The reaction between cellulose and heavy water. Part 1. A qualitative study by infra-red spectroscopy. Trans Faraday Soc 52:481–487

Mann J, Marrinan HJ (1956b) The reaction between cellulose and heavy water. Part 2.—Measurement of absolute accessibility and crystallinity. Trans Faraday Soc 52:487–492

Mann J, Marrinan HJ (1956c) The reaction between cellulose and heavy water. Part 3.—A quantitative study by infra-red spectroscopy. Trans Faraday Soc 52:492–497

Marechal Y, Chanzy H (2000) The hydrogen bond network in Iβ cellulose as observed by infrared spectrometry. J Mol Struct 523:183–196

Marrinan HJ, Mann J (1956) Infrared spectra of the crystalline modifications of cellulose. J Polym Sci 21:301–311. https://doi.org/10.1002/pol.1956.120219812

Matsuoka S, Kawamoto H, Saka S (2011) Thermal glycosylation and degradation reactions occurring at the reducing ends of cellulose during low-temperature pyrolysis. Carbohydr Res 346:272–279. https://doi.org/10.1016/j.carres.2010.10.018

Matsuoka S, Kawamoto H, Saka S (2014) What is active cellulose in pyrolysis? An approach based on reactivity of cellulose reducing end. J Anal Appl Pyrolysis 106:138–146. https://doi.org/10.1016/j.jaap.2014.01.011

Michell AJ, Higgins HG (1999) The Absence of Free Hydroxyl Groups in Cellulose. Cellulose 6:89–91. https://doi.org/10.1023/A:1009258732505

Müller M, Czihak C, Schober H, et al (2000) All Disordered Regions of Native Cellulose Show Common Low-Frequency Dynamics. Macromolecules 33:1834–1840

Nam S, Hillyer MB, Condon BD (2020) Method for identifying the triple transition (glass transition-dehydration-crystallization) of amorphous cellulose in cotton. Carbohydr Polym 228:115374. https://doi.org/10.1016/j.carbpol.2019.115374

Nevell TP, Upton WR (1976) The hydrolysis of cotton cellulose by hydrochloric acid in benzene. Carbohydr Res 49:163–174. https://doi.org/10.1016/S0008-6215(00)83134-1

Newman RH (2008) Simulation of X-ray diffractograms relevant to the purported polymorphs cellulose IVI and IVII. Cellulose 15:769–778. https://doi.org/10.1007/s10570-008-9225-5

Newman RH (2004) Carbon-13 NMR evidence for cocrystallization of cellulose as a mechanism for hornification of bleached kraft pulp. Cellulose 11:45–52. https://doi.org/10.1023/B:CELL.0000014768.28924.0c

Newman RH, Hill SJ, Harris PJ (2013) Wide-Angle X-Ray Scattering and Solid-State Nuclear Magnetic Resonance Data Combined to Test Models for Cellulose Microfibrils in Mung Bean Cell Walls. Plant Physiol 163:1558–1567. https://doi.org/10.1104/pp.113.228262

Niinivaara E, Arshath SAA, Nieminen K, et al (2018) The Effect of Polymorphism on the Kinetics of Adsorption and Degradation: A Case of Hydrogen Chloride Vapor on Cellulose. Adv Sustain Syst 2:1800026. https://doi.org/10.1002/adsu.201800026

Nishiyama Y, Isogai A, Okano T, et al (1999) Intracrystalline deuteration of native cellulose. Macromolecules 32:2078–2081

Nishiyama Y, Johnson GP, French AD (2012) Diffraction from nonperiodic models of cellulose crystals. Cellulose 19:319–336. https://doi.org/10.1007/s10570-012-9652-1

Nishiyama Y, Kim U-J, Kim D-Y, et al (2003) Periodic Disorder along Ramie Cellulose Microfibrils. Biomacromolecules 4:1013–1017. https://doi.org/10.1021/bm025772x

Nyström G, Arcari M, Adamcik J, et al (2018) Nanocellulose Fragmentation Mechanisms and Inversion of Chirality from the Single Particle to the Cholesteric Phase. ACS Nano. https://doi.org/10.1021/acsnano.8b00512

O'Connor RT, DuPré EF, Mitcham D (1958) Applications of Infrared Absorption Spectroscopy to Investigations of Cotton and Modified Cottons. Text Res J 28:382–392. https://doi.org/10.1177/004051755802800503

Olsson A-M, Salmén L (2004) The association of water to cellulose and hemicellulose in paper examined by FTIR spectroscopy. Carbohydr Res 339:813–818. https://doi.org/10.1016/j.carres.2004.01.005

Pääkkönen T, Spiliopoulos P, Knuts A, et al (2018) From vapour to gas: optimising cellulose degradation with gaseous HCl. React Chem Eng. https://doi.org/10.1039/C7RE00215G

Panaitescu A, Grason GM, Kudrolli A (2017) Measuring geometric frustration in twisted inextensible filament bundles. Phys Rev E 95:052503. https://doi.org/10.1103/PhysRevE.95.052503

Papadopoulos J, Chen C-L, Goldstein IS (2009) The Behavior of Lignin during Hydrolysis of Sweetgum Wood with Concentrated Hydrochloric Acid at Moderate Temperatures. Holzforsch - Int J Biol Chem Phys Technol Wood 35:283–286. https://doi.org/10.1515/hfsg.1981.35.6.283

Pastorova I, Botto RE, Arisz PW, Boon JJ (1994) Cellulose char structure: a combined analytical Py-GC-MS, FTIR, and NMR study. Carbohydr Res 262:27–47. https://doi.org/10.1016/0008-6215(94)84003-2

Pouteau C, Cathala B, Dole P, et al (2005) Structural modification of Kraft lignin after acid treatment: characterisation of the apolar extracts and influence on the antioxidant properties in polypropylene. Ind Crops Prod 21:101–108. https://doi.org/10.1016/j.indcrop.2004.01.003

Priest DJ, Shimell RJ (1963) Determination of the accessibility of cellulose films by infra-red spectroscopy. J Appl Chem 13:383–391. https://doi.org/10.1002/jctb.5010130903

Ramírez B, Bucio L (2018) Microcrystalline cellulose (MCC) analysis and quantitative phase analysis of ciprofloxacin/MCC mixtures by Rietveld XRD refinement with physically based background. Cellulose 25:2795–2815. https://doi.org/10.1007/s10570-018-1761-z

Rånby BG, Banderet A, Sillén LG (1949) Aqueous Colloidal Solutions of Cellulose Micelles. Acta Chem Scand 3:649–650. https://doi.org/10.3891/acta.chem.scand.03-0649

Reishofer D, Spirk S (2015) Deuterium and Cellulose: A Comprehensive Review. In: Rojas OJ (ed) Cellulose Chemistry and Properties: Fibers, Nanocelluloses and Advanced Materials. Springer International Publishing, pp 93–114

Rousselle M-A, Nelson ML (1971) Accessibility of Cotton Cellulose by Deuterium Exchange. Text Res J 41:599–604. https://doi.org/10.1177/004051757104100708

Schwanninger M, Rodrigues JC, Pereira H, Hinterstoisser B (2004) Effects of short-time vibratory ball milling on the shape of FT-IR spectra of wood and cellulose. Vib Spectrosc 36:23–40

Segal L, Creely JJ, Martin AE, Conrad CM (1959) An empirical method for estimating the degree of crystallinity of native cellulose using the X-ray diffractometer. Text Res J 29:786–794

Sepall O, Mason SG (1961) Hydrogen exchange between cellulose and water: II. Interconversion of accessible and inaccessible regions. Can J Chem 39:1944–1955

Strømme M, Mihranyan A, Ek R, Niklasson GA (2003) Fractal Dimension of Cellulose Powders Analyzed by Multilayer BET Adsorption of Water and Nitrogen. J Phys Chem B 107:14378–14382. https://doi.org/10.1021/jp034117w

Suchy M, Virtanen J, Kontturi E, Vuorinen T (2010) Impact of Drying on Wood Ultrastructure Observed by Deuterium Exchange and Photoacoustic FT-IR Spectroscopy. Biomacromolecules 11:515–520. https://doi.org/10.1021/bm901268j

Thybring EE, Thygesen LG, Burgert I (2017) Hydroxyl accessibility in wood cell walls as affected by drying and re-wetting procedures. Cellulose 24:2375–2384

Thygesen A, Oddershede J, Lilholt H, et al (2005) On the determination of crystallinity and cellulose content in plant fibres. Cellulose 12:563–576. https://doi.org/10.1007/s10570-005-9001-8

Usov I, Nyström G, Adamcik J, et al (2015) Understanding nanocellulose chirality and structure–properties relationship at the single fibril level. Nat Commun 6:7564. https://doi.org/10.1038/ncomms8564

Viëtor RJ, Mazeau K, Lakin M, Pérez S (2000) A priori crystal structure prediction of native celluloses. Biopolymers 54:342–354

Wada M (2002) Lateral thermal expansion of cellulose Iβ and IIII polymorphs. J Polym Sci Part B Polym Phys 40:1095–1102. https://doi.org/10.1002/polb.10166

Wada M, Heux L, Sugiyama J (2004) Polymorphism of Cellulose I Family: Reinvestigation of Cellulose IVI. Biomacromolecules 5:1385–1391

Wada M, Hori R, Kim U-J, Sasaki S (2010) X-ray diffraction study on the thermal expansion behavior of cellulose Iβ and its high-temperature phase. Polym Degrad Stab 95:1330–1334. https://doi.org/10.1016/j.polymdegradstab.2010.01.034

Wadehra IL, Manley RStJ (1965) Irreversible exchange of hydrogen in the drying of cellulose at high temperature. J Appl Polym Sci 9:3499–3502. https://doi.org/10.1002/app.1965.070091026

Watanabe A, Morita S, Kokot S, et al (2006a) Drying process of microcrystalline cellulose studied by attenuated total reflection IR spectroscopy with two-dimensional correlation spectroscopy and principal component analysis. J Mol Struct 799:102–110. https://doi.org/10.1016/j.molstruc.2006.03.018

Watanabe A, Morita S, Ozaki Y (2006b) Study on Temperature-Dependent Changes in Hydrogen Bonds in Cellulose Iβ by Infrared Spectroscopy with Perturbation-Correlation Moving-Window Two-Dimensional Correlation Spectroscopy. Biomacromolecules 7:3164–3170. https://doi.org/10.1021/bm0603591

Watanabe A, Morita S, Ozaki Y (2006c) Temperature-dependent structural changes in hydrogen bonds in microcrystalline cellulose studied by infrared and near-infrared spectroscopy with perturbation-correlation moving-window two-dimensional correlation analysis. Appl Spectrosc 60:611–618

Yu H, Qin Z, Liang B, et al (2013) Facile extraction of thermally stable cellulose nanocrystals with a high yield of 93% through hydrochloric acid hydrolysis under hydrothermal conditions. J Mater Chem A 1:3938–3944

Supplementary information

1. *Preparation of the flax shives*
   a. *Materials and methods*

Cellulose isolation

Prior to hydrolysis, the shive meal was pre-treated in order to separate the cellulose from the other non-cellulosic components following a chlorine-free procedure described elsewhere.(Jiang and Hsieh 2015) The isolation procedure started with a dewaxing step in a Soxhlet apparatus with toluene-ethanol (2:1, v/v) for 20 h. The resulting product was filtered and dried at 70 °C for 24h and 103°C for 2h. Dewaxed shives (FS_d) were obtained. FS_d were then treated with NaOH (5 wt.%) for 24 h at room temperature and 5 h at 90°C. Shives were then sequentially filtered and washed 3 times in order to obtain clear filtrates with a neutral pH. After neutralization, the flax shives were dried at 70°C for 24 h and at 103°C for 2 h. The shives obtained are called FS_{NaOH}. Bleaching was then performed for 6h at 45 °C with hydrogen peroxide (4%) at a pH of 11.5 adjusted with NaOH. The treated material was filtered, neutralized and dried using the same protocol as that described in the previous step. The shives obtained at the end of this step are called bleached flax shives (FS_b), or cellulose in the rest of this work.

Yield

Aliquots (30 ml) were sampled from the CNC suspensions (~3 g.L^{-1}) and left to dry under a fume hood. The effectiveness of the drying was controlled by measuring the dried CNC powders three times at half-day intervals. The weight of the dry residue was then used to estimate the yield of the hydrolysis expressed as the dry mass of CNC relative to the initial mass of bleached flax shives before hydrolysis.

Microscopy of the flax shives and stems

Flax stems were embedded in paraffin and microtomed sections (~2-3 µm in thickness) were observed in transmission mode using cross-polarizers with an Olympus BX51 optical microscope. The ground flax shives were observed with a field-emission scanning electron microscope (FE-SEM) Hitachi S3000N, in back-scattered electrons mode (BSE) under partial vacuum (5 Pa) with a 15 kV accelerating voltage. The samples were carbon-coated using an automated carbon coated JEC-530 (JEOL Tokyo, Japan) with a preset cycle (6s, 40 V, 2 cycles).

Infrared spectroscopy

FTIR spectra of all the samples were obtained using an attenuated total reflectance Fourier-transform infrared spectroscopy (ATR-FTIR, Frontier, Perkin Elmer). Spectra were collected at ambient temperature from an accumulation of 32 scans at 2 cm^{-1} resolution over the 4000-650 cm^{-1} region. For each sample, 3 spectra were collected, baseline corrected, normalized and averaged (using Spekwin32) in order to obtain a final spectrum for each treatment step.

X-ray diffraction

The diffractograms of the samples before and after bleaching were measured. Powder diffractograms were acquired in reflection mode with a θ-θ Bragg-Brentano configuration using an Xpert-Pro Powder (PANalytical B.V., Almelo, Nederland) with a cobalt radiation

source ($\lambda_{CoK\alpha}$ = 1.790307 Å) and a PIXcel 1D detector. The operating voltage and current were maintained at 40 kV and 40 mA, respectively. Measurements were made between 10 and 90° with 0.0525° steps and for a total duration of 3.5 h. The lateral divergence of the incident beam path was controlled with 0.04° Soller slits and a 15 mm mask and its divergence in the 2.θ plane was controlled with a ½° programmable divergence slit and a 1° fixed anti-scatter slit. The crystallite lateral thickness in the direction perpendicular to the (200) plane was estimated using Scherrer equation (K=0.9) and the crystallinity index (*Crl*) was calculated following the work of Segal (1959).(Segal et al. 1959; Guinier 1963; Duchemin et al. 2007)

13C CP/MAS NMR spectroscopy

Solid-state ^{13}C CP/MAS NMR experiments were performed on a Bruker AV III 400 spectrometer with a ^{13}C resonance frequency of 100.66 MHz, equipped with a Bruker 4 mm double resonance probe. The spectra were obtained at spinning rate of 12 KHz and 12,288 transients were added with a recycling delay of 1.5 s. A contact time of 2,000 ms was employed. The ^{13}C chemical shifts were referenced to TMS.

b.   Results
Microscopy and yield

Flax shives are part of the flax stem and they are produced by scutching the flax stems during the production of textile fibers. They mainly consist of xylem residues. Polarized optical microscopy of flax stem cross-sections evidences the presence of crystalline cellulose in the xylem because of its birefringence (Figure S5). Therefore, this cheap material was deemed as a possible source for the production of CNC. The starting material was ground to a fine powder in order to render the two main subsequent treatments (bleaching and hydrolysis) as homogeneous as possible. SEM (Figure S5b) shows elongated fragments 25-80 µm in length and 8-12 µm in diameter.
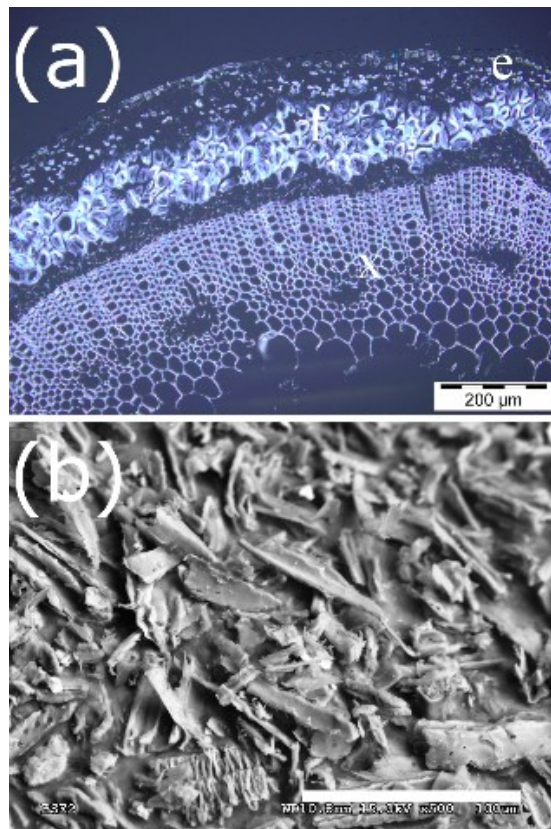

Figure S1. Polarized optical microscopy (a) of a flax stem displaying the epidermis (e), the fibers (f) and the xylem (x); SEM micrographs (b) of the ground flax shives used in this work (scale bar: 100 µm).

27

The flax shives that were received underwent a chlorine-free bleaching treatment in three steps. The yields of the Soxhlet extraction, NaOH treatment and bleaching step were respectively 91 wt.%, 55 wt.% and 54 wt.% (with respect to the initial weight). At the end of the final step, the total yield was slightly more to that usually found in the literature: it is admitted that flax shives contain 34-53 wt.% cellulose, 23-31 wt.% lignin and 13-26 wt.% hemicellulose as well as moderate amounts of ash (1-2 wt.%) and wax (3-4 wt.%).(Sain and Fortier 2002; Kim and Mazza 2009; del Río et al. 2011)

ATR-FTIR

ATR-FTIR of the bleached material confirm the presence of cellulose with typical cellulose I bands (Figure S6). The distinctive carbonyl band of hemicellulose at 1732 cm^{-1} was removed. This band can sometimes be found in glucomannan, xyloglucan or glucuronic acid-substituted xylan. The disappearance of this band coincides with the NaOH treatment step which resulted in a ~36 % weight loss. Since the hemicellulose content is expected to lie in the 13-26 wt.% range, one assumes that most hemicelluloses were removed as well as some other components. The final yield found here (54 wt.%) is in the upper range with respect to the cellulose content expected in flax shives. Possible remnants of cell wall compounds could explain this discrepancy. In particular, a portion of recalcitrant lignin might have resisted the different treatments: ATR-FTIR (Figure S6) shows remaining lignin bands at 1660 cm^{-1} (C=O), 1590 and 1508 cm^{-1} (aromatic skeletal vibration), 1460 cm^{-1} (C-H deformation) and 1265 cm^{-1} (ring stretching).(Marchessault 1962; Pandey 1999; Duarte et al. 2000; Derkacheva and Sukhov 2008; Duchemin and Staiger 2009; Huang et al. 2019) The bands found at 2920 and 2850 cm^{-1} (C-H stretching of aromatic groups) were removed after the Soxhlet extraction. These bands are sometimes attributed to lignin. Given the strong presence of many lignin bands throughout the process and the removal of these two C-H stretching bands in the toluene:ethanol mixture, they were rather assigned to soluble wax compounds.
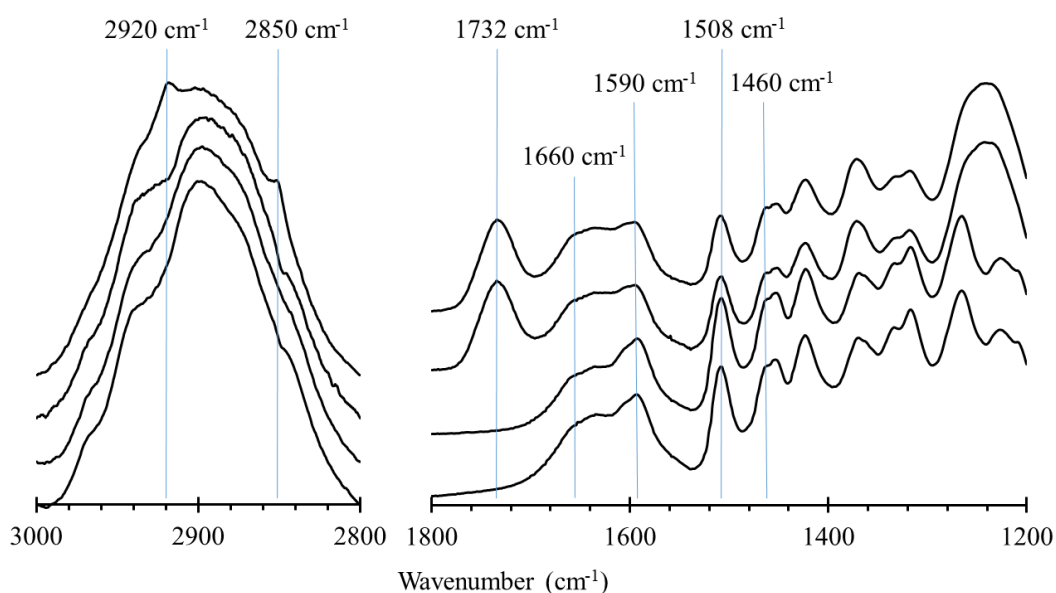

Figure S2. Absorbance FTIR spectra of (top to bottom): the as-received ground flax shives, the shives that were solvent extracted using a Soxhlet apparatus and a toluene:ethanol (2:1) reflux, the shives treated with NaOH and the shives bleached with H_2O_2 in an alkaline environment.

13C CP/MAS NMR spectroscopy

13C CP/MAS NMR spectroscopy is complementary to FTIR spectroscopy and X-ray diffraction with respect to the information provided on cellulose (allomorphic nature, crystallinity, crystallite size) and on the nature of non-cellulosic polysaccharides or phenolic compounds. In this work, two bands were removed by the "bleaching" treatment (Figure S7).

28

These bands are visible on the signal obtained on the as-received flax shives. The first band is a peak near 172 ppm and it is most likely attributed to galacturonan or other various acetyl or carboxyl moieties.(Newman et al. 1996; Jarvis and McCann 2000; Maunu 2002; Martins et al. 2006; Duchemin et al. 2012) the second peak was found at 20.7 ppm and it is assigned to the acetyl group in hemicelluloses (Newman and Hemmingson 1990; Girault et al. 1997; Jarvis and McCann 2000; Maunu 2002; Martins et al. 2006) Therefore, and in accordance with FTIR results, it is reasonable to infer that hemicelluloses and pectins were removed during the pre-treatment step. Other bands remained throughout the process. In particular, several small bands in the 120-160 ppm region with peaks at 151.2, 147.1 and 132.9 ppm remained. These bands are attributed to the C=C bonds in guaiacyl and syringil units.(Josefsson et al. 2001; Maunu 2002; Newman et al. 2005) The lignin peak at 55.5 ppm also remained.(Josefsson et al. 2001; Maunu 2002; Newman et al. 2005) Therefore, the pre-treatment used wasn't able to remove the lignin recalcitrant portion. This result is also in line with FTIR results. Regarding cellulose, all the characteristic bands were present: C-1 near 105 ppm (I_β :104.1 and 105.3 ppm; I_α: 104.7 ppm), C-4 "interior" near 88.5 ppm, C-4 "exterior" with a band at 83.6-83.8 ppm, C-2,3,5 with intense bands near 74.6 and 72.0 ppm and C-6 at 62.4 and 64.6 ppm.(Newman et al. 1996; Larsson et al. 1997; Newman 1999; Maunu 2002)
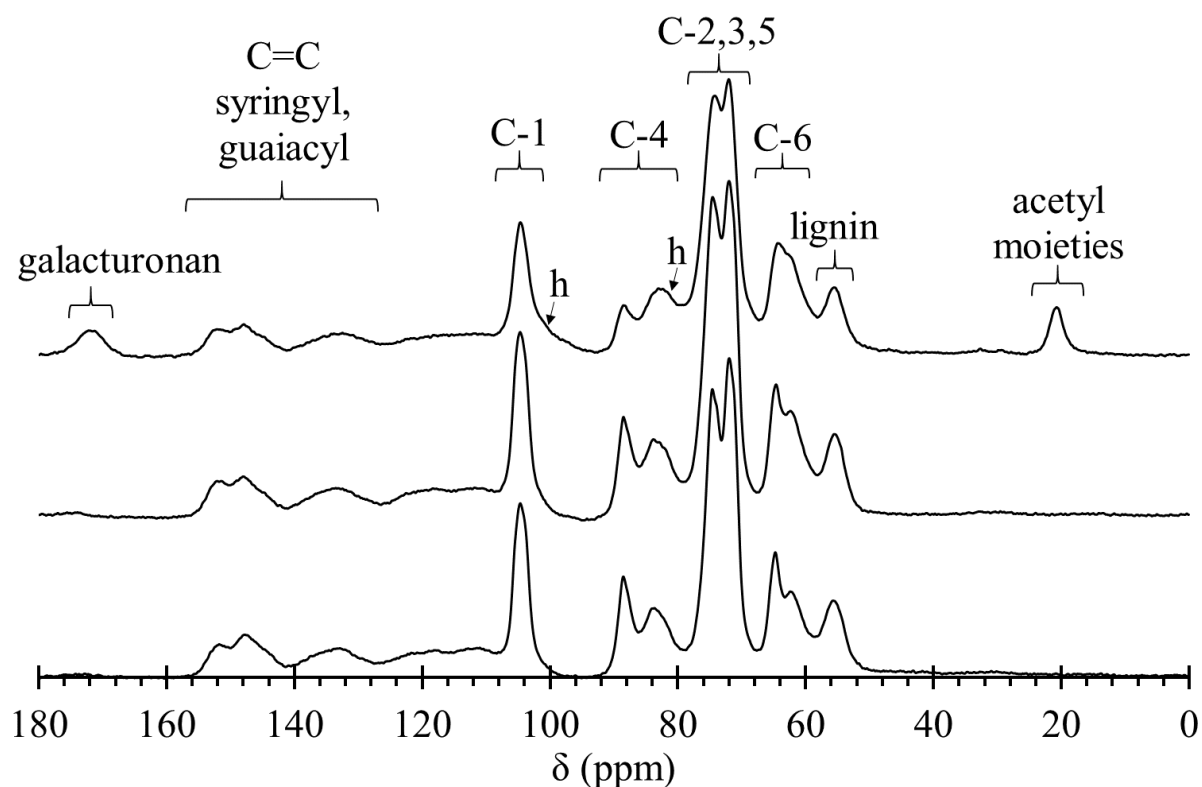

Figure S3. Nuclear magnetic resonance spectra of "raw" ground flax shives (top), the reference non-hydrolyzed sample (middle) and the sample that was hydrolyzed for 8 h (bottom). The C-1 to C-6 carbons are cellulose bands. The "h" letter indicates typical hemicellulose shoulders. All other bands are explicitly attributed.

X-ray diffraction

XRD unambiguously confirms the presence of crystalline cellulose with typical cellulose I diffractograms (Figure S8) and the relatively broad diffractograms indicate the presence of small cellulose crystallites in the flax shives, relatively to that found in cotton, flax fibers or tunicate. The dimensions of the crystallites in the direction orthogonal to the (200) plane were estimated using Scherrer equation. They were found to be ~27 Å initially and ~36 Å after the alkaline treatments (Table S2). It is well-known that NaOH can dissolve very small crystallites and provide extra-mobility to

cellulose oligomers, which translates into an average thickening of the cellulose crystallites left behind such treatments; the removal of non-crystalline components also induces an increased crystallinity (Table S1).(Newman 2004; Daicho et al. 2018) Additionally, one notices the presence of quartz in the sample due to the (101) and (10$\bar{1}$) diffraction peaks at 31° (Figures S8 and 4). Due to the industrial nature of the flax shive extraction process, it is indeed plausible to find small amounts of quartz in the resulting product. An XRD Rietveld analysis using the Maud software was performed (data not shown here) and the amount of quartz in the bleached material was found to be ~0.4 wt.%.
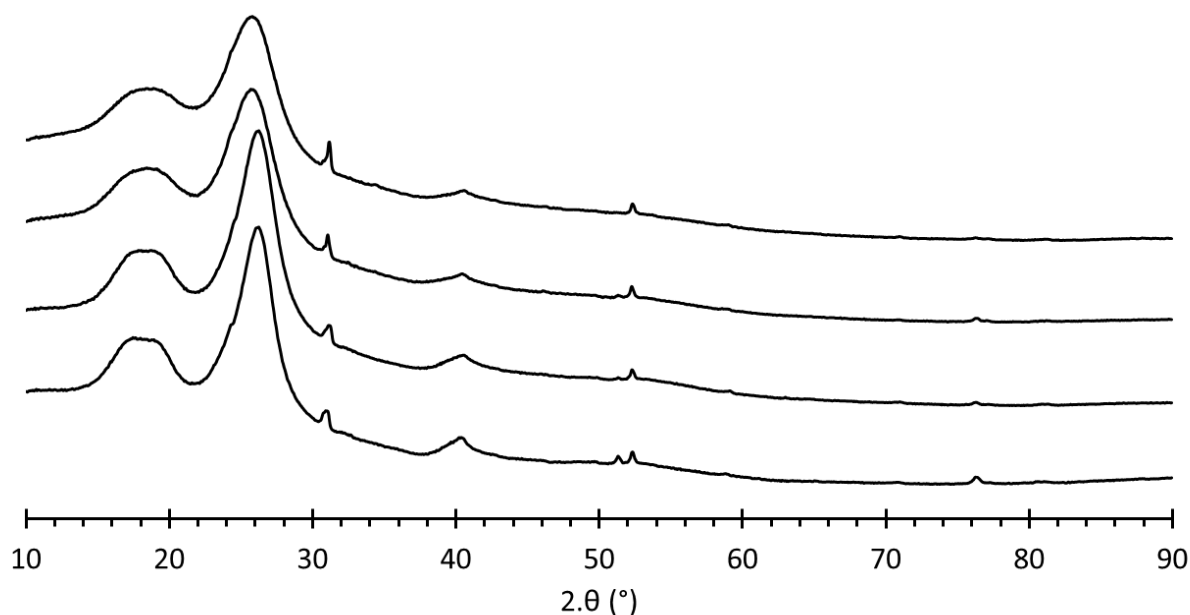
Figure S4. Powder diffractograms of (top to bottom): the as-received ground flax shives, the shives that were solvent extracted using a soxhlet apparatus and a toluene:ethanol (2:1) reflux, the shives treated with NaOH and the shives bleached with H_2O_2 in an alkaline environment.

Table S1. XRD results of the bleaching process

	Raw material	Soxhlet extraction	NaOH treatment	Alkaline H_2O_2	0 h	0.5 h	1 h	2 h	4 h	8 h
(200) peak position (°)	25.856	25.825	26.209	26.182	26.203	26.185	26.175	26.260	26.244	26.147
FWHM (°)	3.470	3.356	2.818	2.647	2.734	2.691	2.696	2.675	2.640	2.641
Size (Å)	27.3	28.2	33.6	35.8	34.7	35.2	35.1	35.4	35.9	35.9
CrI (%)	36	40	53	54	53	55	56	57	57	56

2. Anisotropic size broadening: discrete representation
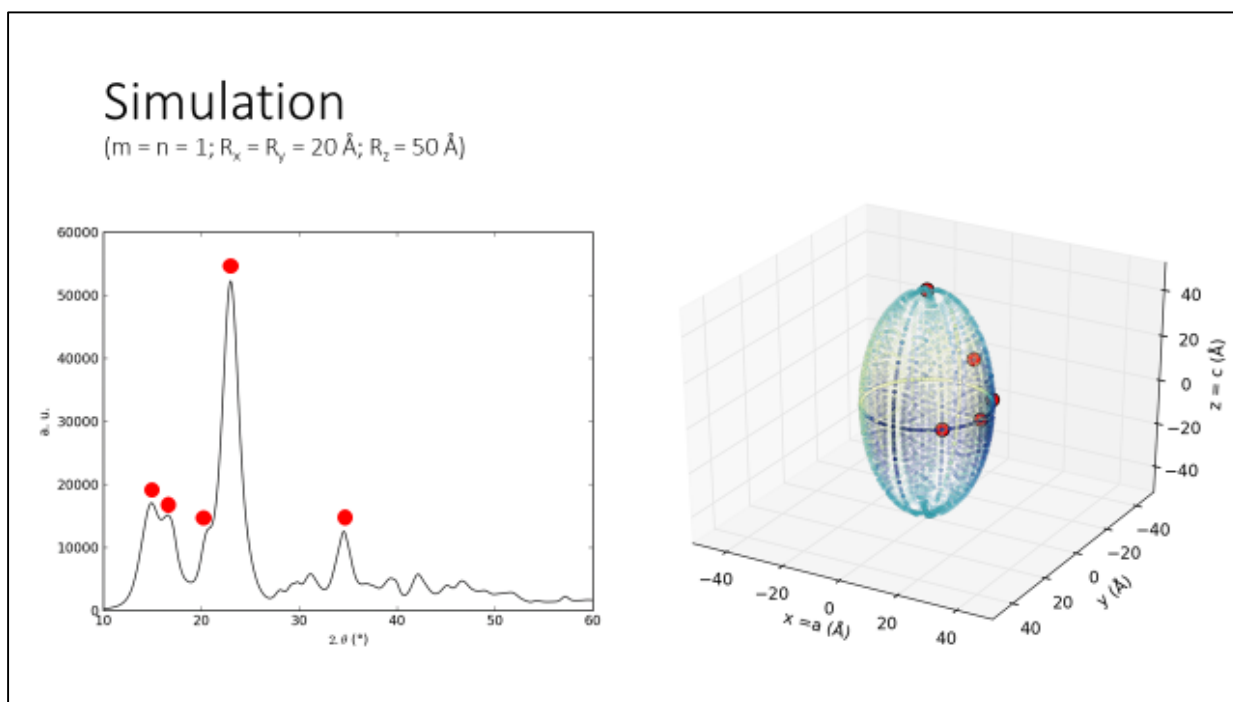
Figure S5. Plot of a "standard" calculated diffractogram (left) and corresponding superellispoid hull (right). The hull is a discrete representation of the points projected on the superellipsoid shape for each (*hkl)* plane. The most intense Bragg bands corresponding to the (110), (1$\bar{1}$0), (102), (200) and (004) planes are materialized by red dots on both figures.

3. Hydrolysis: complementary information
   ^{13}C CP/MAS NMR

The amount of cellulose chains located in the amorphous regions or at the surface of the crystallites was obtained by measuring the area between the baseline and the spectral line between 79 and 86 ppm. The amount of interior chains was estimated as the corresponding area between 86 and 94 ppm. The I_α:I_β ratio was estimated using the three C-1 bands of cellulose in the 100-108 ppm range.(Duchemin et al. 2012) The calculation was based on the relative areas of the phases after a fitting three Gaussian function corresponding to the I_β phase (104.1 and 105.3 ppm) and I_α phase (104.7 ppm).
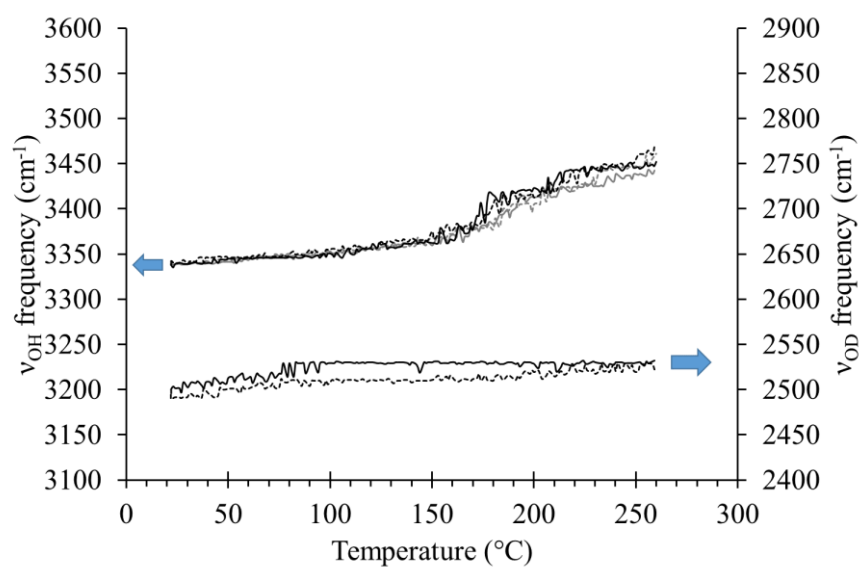
Table S2. RH measurement of the films prior to acid hydrolysis

| Time (h)	0	0,5	1	2	4	8
Water content (w/w)	24,0 %	42,7%	26,8%	29,2%	25,2%	34,1%
Standard deviation	1,9%	3,4%	5,1%	1,9%	4,5%	3,7%
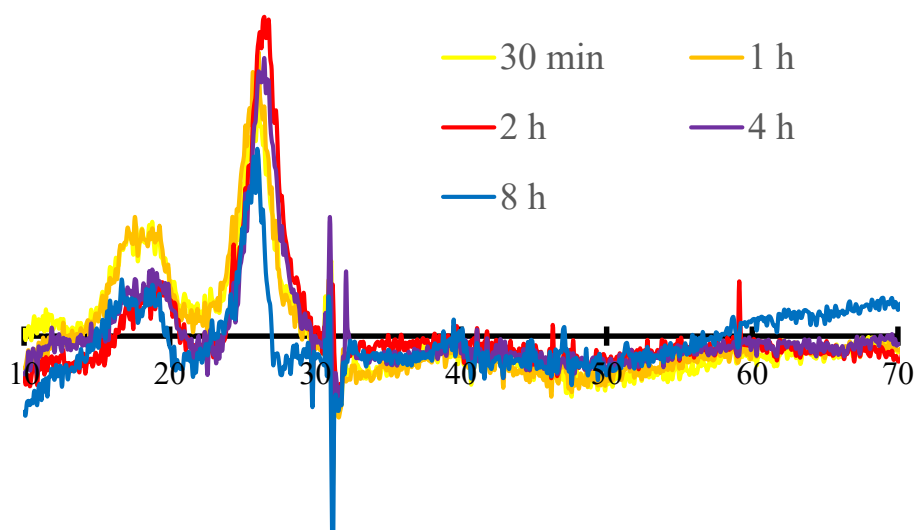
Figure S6. Difference between the area-normalized diffractograms obtained on the hydrolyzed sample and on the non-hydrolyzed reference sample.


Figure S7. Peak positions in the elongational –OH and –OD zones for the reference sample (continuous line) and 8h hydrolyzed sample (dotted line) that were deuterated (black) or reprotonated (grey).
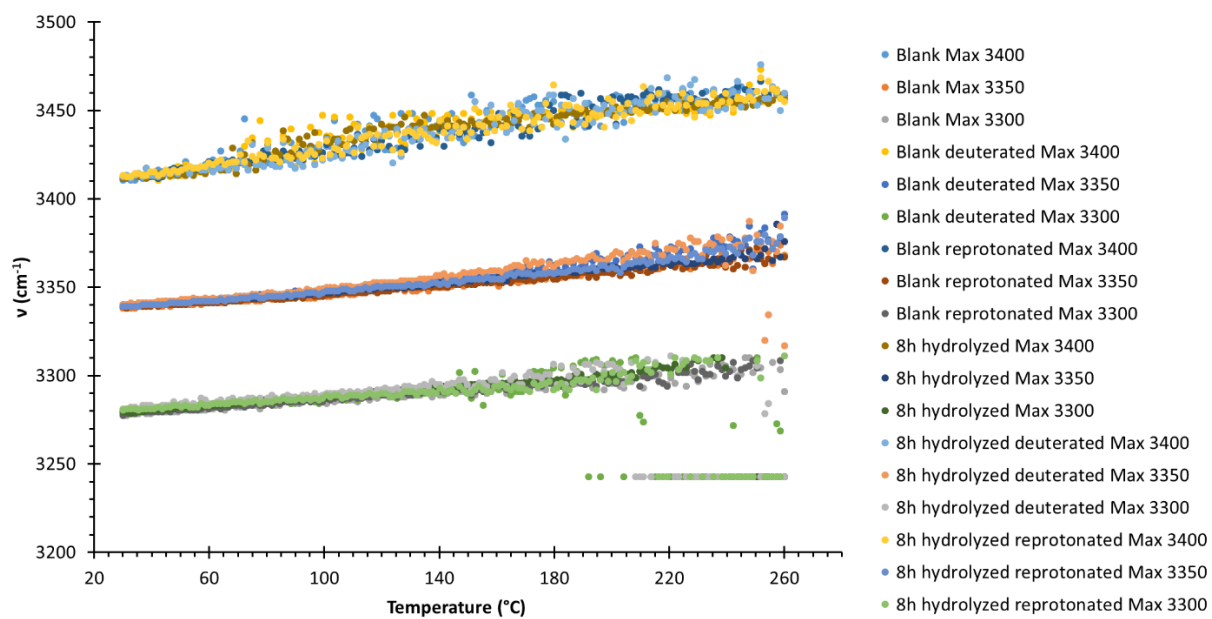
Figure S8. Maxima of the three main hydrogen bond bands as a function of temperature.
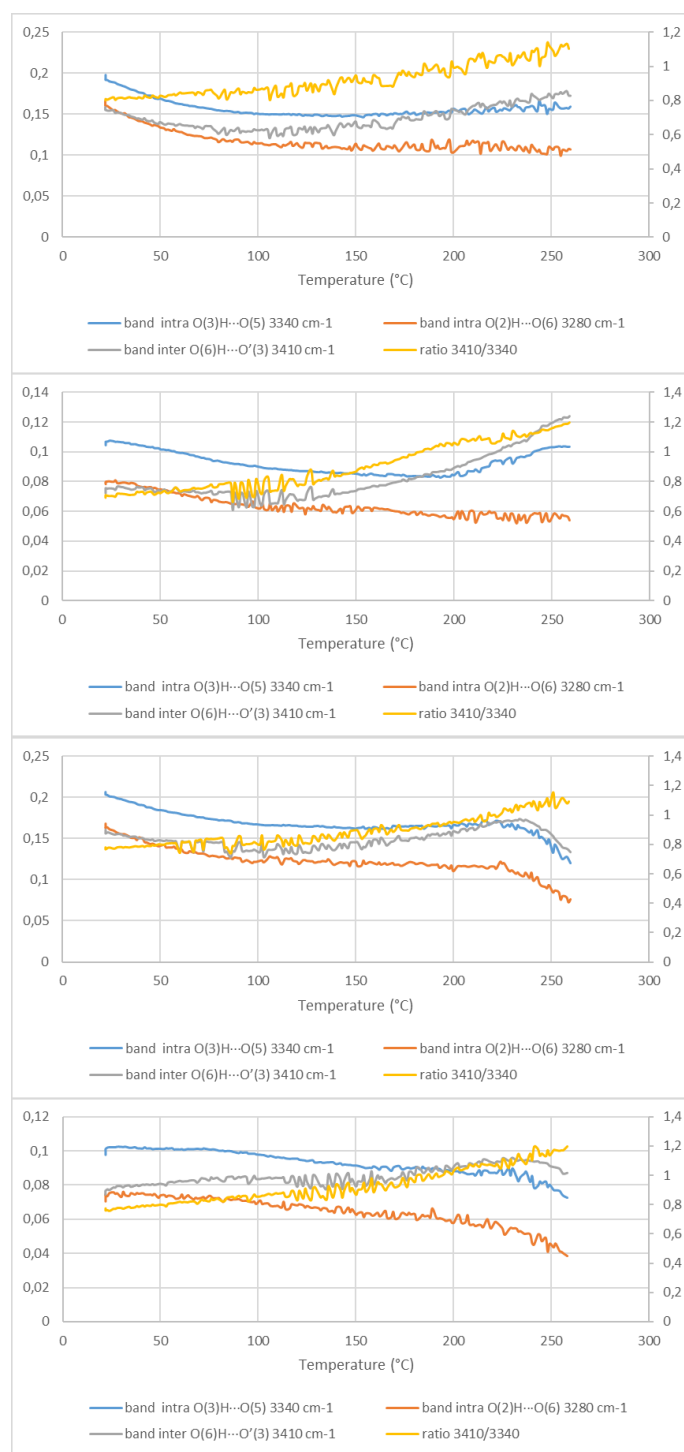
Figure S9. Intensities (a.u.) of the main bands as a function of the temperature for the non-hydrolyzed sample (top row) and the 8 h hydrolyzed samples (bottom row) after the regular process (left column) or after isotopic exchange with D_2O (right column). Intensities are arbitrary units. The ratio (yellow line) is the only data that is reported on the second vertical axis (right) of each graph.
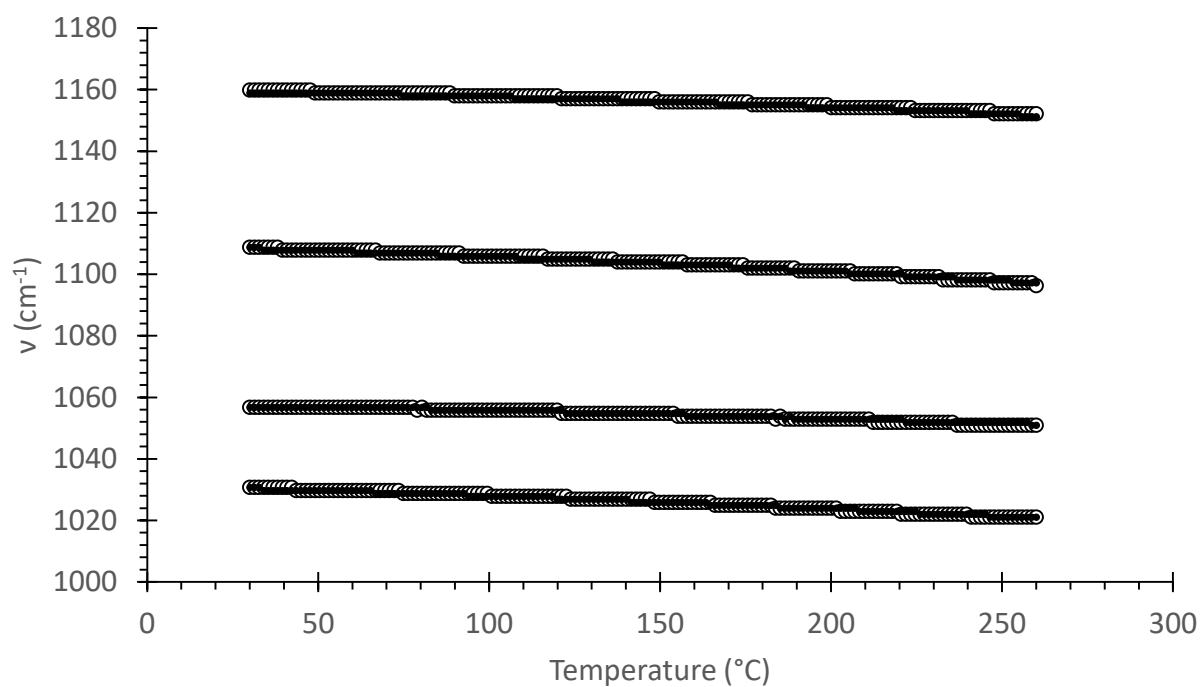
Figure S10. Temperature dependence of the main C-O bands during the heating cycle of the normally protonated non-hydrolyzed sample ($\circ$) and the hydrolyzed sample ($\bullet$).
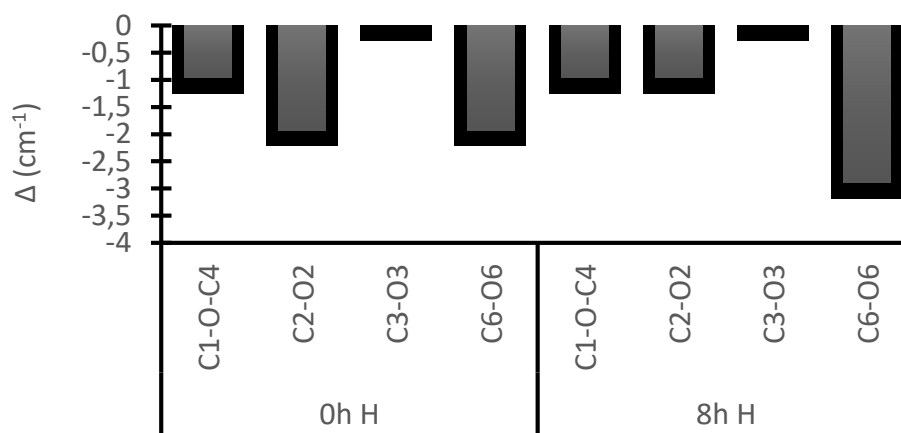
Figure S11. Band shifts of the main C-O bonds after completion of the heating and cooling cycle with respect to the initial position (adapted from Figure 8d).
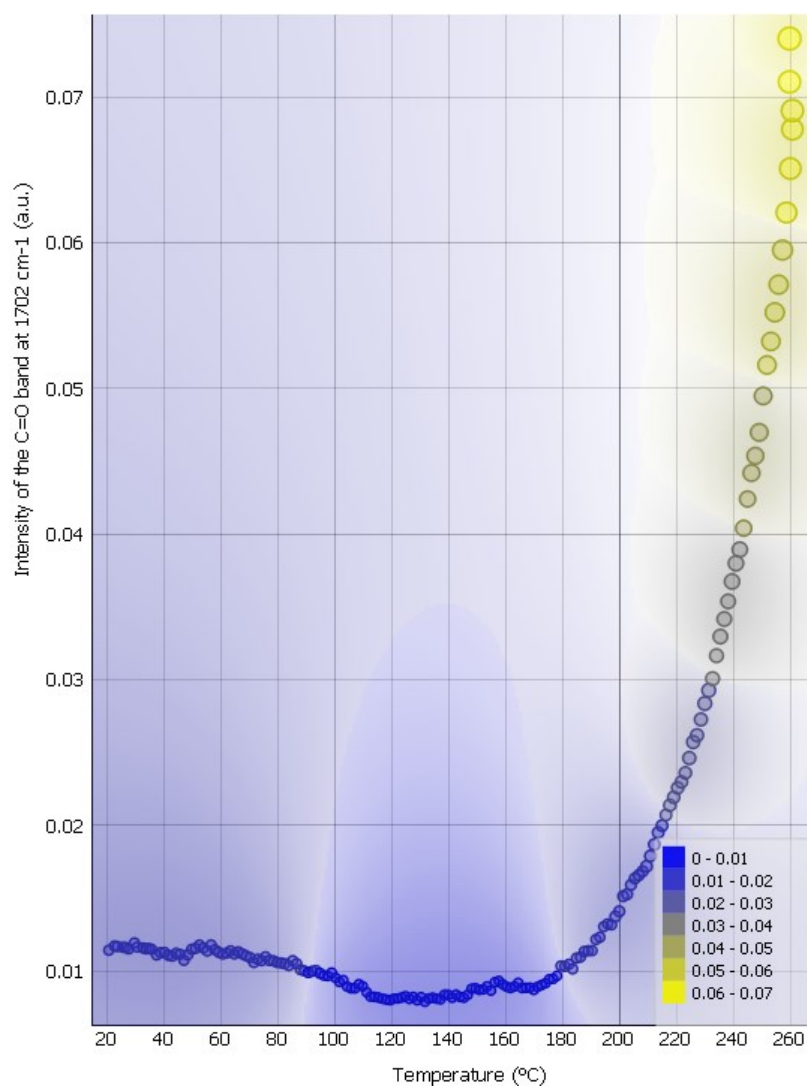
Figure S12. Intensity of the band at 1702 cm^{-1} as a function of temperature (data from Figure 7).
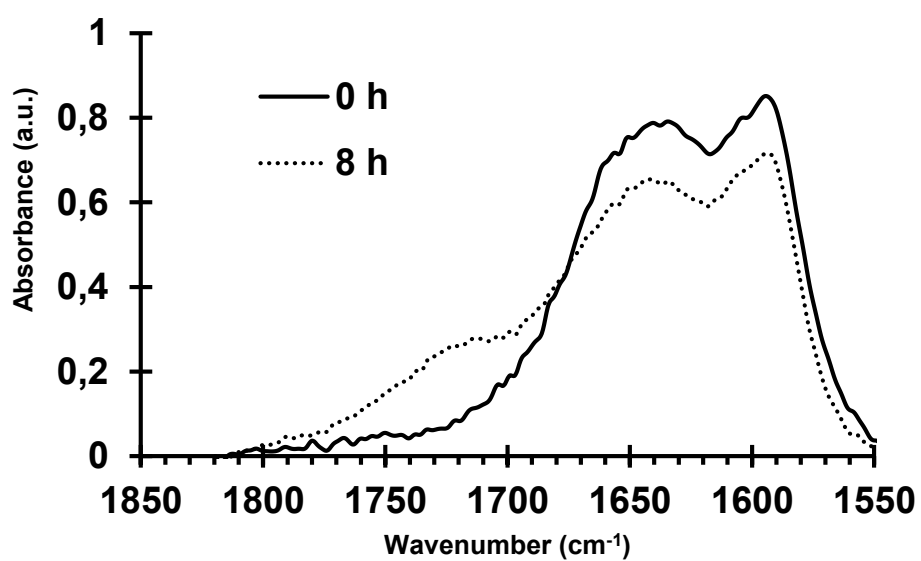
Figure S13. FTIR absorbance spectra of the never deuterated samples in the initial conditions. The molecular water region is plotted after normalization relative to the −CH band at 2900 cm^{-1} (intensity method).

References:

Daicho K, Saito T, Fujisawa S, Isogai A (2018) The Crystallinity of Nanocellulose: Dispersion-Induced Disordering of the Grain Boundary in Biologically Structured Cellulose. ACS Appl Nano Mater. doi: 10.1021/acsanm.8b01438

del Río JC, Rencoret J, Gutiérrez A, et al (2011) Structural Characterization of Guaiacyl-rich Lignins in Flax (Linum usitatissimum) Fibers and Shives. J Agric Food Chem 59:11088–11099. doi: 10.1021/jf201222r

Derkacheva O, Sukhov D (2008) Investigation of Lignins by FTIR Spectroscopy. Macromol Symp 265:61–68. doi: 10.1002/masy.200850507

Duarte AP, Robert D, Lachenal D (2000) Eucalyptus globulus Kraft Pulp Residual Lignins. Part 1. Effects of Extraction Methods upon Lignin Structure. Holzforschung 54:365–372

Duchemin B, Newman R, Staiger M (2007) Phase transformations in microcrystalline cellulose due to partial dissolution. Cellulose 14:311–320

Duchemin B, Staiger MP (2009) Treatment of Harakeke fiber for biocomposites. J Appl Polym Sci 112:2710–2715

Duchemin B, Thuault A, Vicente A, et al (2012) Ultrastructure of cellulose crystallites in flax textile fibers. Cellulose 19:1837–1854. doi: 10.1007/s10570-012-9786-1

Girault R, Bert F, Rihouey C, et al (1997) Galactans and cellulose in flax fibers: putative contributions to the tensile strength. Int J Biol Macromol 21:179–188. doi: 10.1016/S0141-8130(97)00059-7

Guinier A (1963) X-ray diffraction in crystals, imperfect crystals, and amorphous bodies. W. H. Freeman and Company, San Francisco and London

Huang J, Wang M, Song P, et al (2019) Directed 2D nanosheet assemblies of amphiphilic lignin derivatives: Formation of hollow spheres with tunable porous structure. Ind Crops Prod 127:16–25. doi: 10.1016/j.indcrop.2018.10.036

Jarvis MC, McCann MC (2000) Macromolecular biophysics of the plant cell wall: Concepts and methodology. Plant Physiol Biochem 38:1–13. doi: 10.1016/S0981-9428(00)00172-8

Jiang F, Hsieh Y-L (2015) Cellulose nanocrystal isolation from tomato peels and assembled nanofibers. Carbohydr Polym 122:60–68. doi: 10.1016/j.carbpol.2014.12.064

Josefsson T, Lennholm H, Gellerstedt G (2001) Changes in cellulose supramolecular structure and molecular weight distribution during steam explosion of aspen wood. Cellulose 8:289–296

Kim J-W, Mazza G (2009) Extraction and Separation of Carbohydrates and Phenolic Compounds in Flax Shives with pH-Controlled Pressurized Low Polarity Water. J Agric Food Chem 57:1805–1813. doi: 10.1021/jf803467y

Larsson PT, Wickholm K, Iversen T (1997) A CP/MAS13C NMR investigation of molecular ordering in celluloses. Carbohydr Res 302:19–25

Marchessault RH (1962) Application of infra-red spectroscopy to cellulose and wood polysaccharides. Pure Appl Chem 5:107–129

Martins MA, Forato LA, Mattoso LHC, Colnago LA (2006) A solid state 13C high resolution NMR study of raw and chemically treated sisal fibers. Carbohydr Polym 64:127–133

Maunu SL (2002) NMR studies of wood and wood product. Prog Nucl Magn Reson Spectrosc 40:151–174

Newman RH (1999) Estimation of the relative proportions of cellulose Iα and Iβ in wood by carbon-13 NMR spectroscopy. Holzforschung 53:335–340

Newman RH (2004) Carbon-13 NMR evidence for cocrystallization of cellulose as a mechanism for hornification of bleached kraft pulp. Cellulose 11:45–52. doi: 10.1023/B:CELL.0000014768.28924.0c

Newman RH, Davies LM, Harris PJ (1996) Solid-State 13C Nuclear Magnetic Resonance Characterization of Cellulose in the Cell Walls of Arabidopsis thaliana Leaves. Plant Physiol 111:475–485

Newman RH, Hemmingson JA (1990) Determination of the degree of cellulose crystallinity in wood by carbon-13 nuclear magnetic resonance spectroscopy. Holzforschung 44:351

Newman RH, Tauwhare SEK, Scheele S, Kanawa RT (2005) Leaf-fibre lignins of Phormium varieties compared by solid-state 13C NMR spectroscopy. Holzforschung 59:147–152

Pandey KK (1999) A study of chemical structure of soft and hardwood and wood polymers by FTIR spectroscopy. J Appl Polym Sci 71:1969–1975

Sain M, Fortier D (2002) Flax shives refining, chemical modification and hydrophobisation for paper production. Ind Crops Prod 15:1–13. doi: 10.1016/S0926-6690(01)00090-5

Segal L, Creely JJ, Martin AE, Conrad CM (1959) An empirical method for estimating the degree of crystallinity of native cellulose using the X-ray diffractometer. Text Res J 29:786–794